

# Extension of the Liège Intranuclear-Cascade model to reactions induced by light nuclei

Daive Mancusi,<sup>1,\*</sup> Alain Boudard,<sup>1,†</sup> Joseph Cugnon,<sup>2</sup>  
Jean-Christophe David,<sup>1,‡</sup> Pekka Kaitaniemi,<sup>1,†</sup> and Sylvie Leray<sup>1</sup>  
<sup>1</sup>*CEA, Centre de Saclay, Irfu/SPhN, F-91191 Gif-sur-Yvette, France*  
<sup>2</sup>*Fundamental Interactions in Physics and Astrophysics,  
University of Liège, allée du 6 août 17, bât. B5, B-4000 Liège 1, Belgium*  
(Dated: August 6, 2018)

The purpose of this paper is twofold. First, we present the extension of the Liège Intranuclear Cascade model to reactions induced by light ions. We describe here the ideas upon which we built our treatment of nucleus-nucleus reactions and we compare the model predictions against a vast set of heterogeneous experimental data. In spite of the discussed limitations of the intranuclear-cascade scheme, we find that our model yields valid predictions for a number of observables and positions itself as one of the most attractive alternatives available to Geant4 users for the simulation of light-ion-induced reactions. Second, we describe the C++ version of the code, which it is physics-wise equivalent to the legacy version, is available in Geant4 and will serve as the basis for all future development of the model.

PACS numbers: 24.10.Lx, 25.40.Sc, 25.70.-z, 25.70.Mn

Keywords: spallation reactions; intranuclear cascade; light-ion-induced reactions; nucleus-nucleus reactions

## I. INTRODUCTION AND MOTIVATION

Reactions involving light ions (defined as  $A \leq 18$  for the purpose of this paper) play an important role in several applications. In hadrontherapy, for instance, cancer patients are treated using accelerated beams of protons or light ions [1]. Nuclear reactions between the beam particles and the body of the patient can be responsible for dose deposition outside the clinical target volume, which is undesirable. Moreover, it has been demonstrated that the production of  $\beta^+$  emitters in nuclear reactions can be profitably employed to monitor dose deposition in proton [2] or carbon treatment [3].

The radiation environment in space also involves energetic protons and heavy ions [4]. The Galactic Cosmic Rays are one of the contributing sources to radiation in the Solar System; their hadronic component mainly consists of protons and alpha particles, but ions as heavy as iron are known to yield sizable contributions to the equivalent dose absorbed by space crews. Shielding against cosmic radiation relies on nuclear reactions to reduce the health hazard.

Light-ion-induced nuclear reactions are also involved in the production of beams of unstable nuclei. The in-flight projectile-fragmentation method [5] is often realized using  $^9\text{Be}$  production targets. Radioactive beams produced with the ISOL method [6] typically rely on light charged particles (LCPs) to induce spallation or fission in the production target. In either case, the luminosity of the secondary beam crucially depends on the fragment yields in light-ion-induced reactions.

Reactions on light nuclei are also often used in fundamental research at the limits of nuclear stability, for instance in the quest for very neutron-rich or neutron-poor residues [e.g. 7, 8]. Light targets are also employed to extract information about the properties of exotic nuclei from their response to dynamical solicitation [e.g. 9]; see also the work described in Ref. 10, which is particularly relevant to our subject because it was performed with a preliminary version of the model described in the present paper.

The applications listed above typically involve projectile energies of the order of a few tens to several hundreds or even thousands of MeV per nucleon. Since a great deal of reaction channels are open in this energy regime, it is unfeasible to conduct systematic and comprehensive measurement campaigns for all the relevant observables. Semi-empirical deterministic transport codes [e.g. 11, 12] and hadrontherapy-targeted treatment-planning systems [e.g. 13] can be constructed around a restricted number of measured observables. Such codes are usually sufficient to ensure adequate reproduction of the existing data; however, their predictive power is essentially limited to the selected observables in a restricted regime. Thus, there is a need for predictive, physics-based nuclear-reaction models that can be used as all-round tools at the bleeding edge of fundamental and applied research.

Above some 100 MeV incident energy, the nucleon-nucleus reaction dynamics can be described as a sequence of independent nucleon-nucleon interactions taking place in a common mean-field potential [14, 15]. This approximation gives rise to the intranuclear-cascade (INC) class of models, which help shed some light on the reaction mechanism and have proven predictive even below their nominal low-energy limit of validity. In particular, the Liège Intranuclear Cascade (INCL) [16], coupled with the ABLA07 statistical de-excitation code [17], has been

---

\* Member of the Geant4 collaboration; corresponding author. E-mail address: [davide.mancusi@cea.fr](mailto:davide.mancusi@cea.fr)

† Former member of the Geant4 collaboration.

‡ Member of the Geant4 collaboration.

recognized as one of the most accurate models available on the market by the Benchmark of Spallation Models [18], an intercomparison of event generators for nucleon-induced reactions in the 60–3000 MeV incident-energy range, organized under the auspices of the IAEA. The INCL model is a full Monte-Carlo event generator written in Fortran77. The latest version of the Fortran77 code is named INCL4.6 and it is described in detail in recent publications [16]. As such, it represents an ideal starting point for an extension to reactions induced by light ions. A simple extension to light-ion-induced reactions, based on an old Fortran77 version of the model, was attempted a few years ago [19]. The model yielded promising physical results, but maintaining the code quickly grew to the proportions of a formidable task. This was mainly due to the fact that the Fortran77 version was monolithic, hardly flexible and not very legible from the start. This is one of the motivations that has led us to redesign the INCL code from scratch and cast it in modern, object-oriented C++.

Before describing the light-ion extension, we need to define the framework of the model and introduce the C++ redesign of the INCL code, named INCL++ (Section II). The physics of the new code is substantially equivalent to the reference Fortran77 version INCL4.6 for nucleon- and pion-induced reactions; the few minor differences will be highlighted in section II A. We then introduce the extension of the INCL++ model to light-ion-induced reactions (section II B). The differences between INCL++ and the legacy Fortran INCL code are highlighted in Section III. The predictions of the light-ion extension are compared with a variety of experimental data in Section IV. We collect our conclusions in section V. Some Geant4-specific information about the use of INCL++ within this particle-transport toolkit are given as an appendix.

## II. MODEL DESCRIPTION

The Liège Intranuclear Cascade model (INCL) [16, official web site: <http://irfu.cea.fr/Sphn/Spallation/incl.html>] is one of the most refined existing tools for the description of nucleon- and pion-induced reactions in the 50–3000-MeV incident-energy range. The model is currently maintained and jointly developed by the University of Liège (Belgium) and CEA-Saclay (France).

In this framework, the high-energy projectile initiates an avalanche of binary collisions within the target nucleus. Particles (nucleons and pions) are assumed to move in a spherical calculation volume, whose radius  $R_{\max}$  is defined to be large enough to intersect essentially all impact parameters leading to inelastic reactions. Binary particle-particle collisions are subject to Pauli blocking. Emission of nucleons, pions and light clusters is possible; light clusters, in particular, are produced via a dynamical phase-space coalescence algorithm. The cas-

cade stops when the remnant nucleus shows signs of thermalization; a rather unique aspect of INCL is the self-consistent determination of the cascade stopping time. The INCL model is not to be considered as adjustable. It does contain parameters, but they are either taken from known phenomenology (such as the matter density radius of the nuclei) or have been adjusted once for all (such as the parameters of the Pauli blocking or those that determine the coalescence module for the production of the light charged clusters). The validity of the INCL model in the 50–3000-MeV incident-energy range has been extensively demonstrated by the “Benchmark of Spallation Models” [18], sponsored by IAEA.

We now turn to the description of the details that are specific to the INCL++ model. In what follows, and unless otherwise specified, we shall refer to INCL++ v5.1.14, which is the version that was released to the public along with Geant4 v10.0 in December 2013. Subsequent patches to Geant4 v10.0 introduce very few changes to the core of the model. More detailed information about INCL++ in Geant4 are presented as an appendix to the present paper.

### A. Differences with INCL4.6

We try to limit our description to those aspects of INCL++ that are different from the reference Fortran version, INCL4.6 [16]. In some cases, however, a brief presentation of the reference model needs to be included, for clarity’s sake.

We mentioned above that INCL++ was designed to be physically equivalent to INCL4.6 as far as nucleon- and pion-induced reactions are concerned. Nevertheless, in some cases we deliberately chose to introduce some minor difference for the sake of simplicity or consistency. In particular, the treatment of pions in the two codes notably differs for the following details.

First, the radius of the pion potential in INCL4.6 is taken to be  $R_{\pi} = (R_0 + R_{\max})/2$ , where  $R_0$  represents the surface half-density radius and  $R_{\max}$  is the radius of the calculation volume. This means that pions are assumed to quit the INC at  $r = R_{\pi}$ ; however, incoming pions still enter at  $r = R_{\max}$ . This would pose some problems of consistency in the stricter INCL++ code. Thus, for simplicity, pions in INCL++ always enter and leave their potential (and the calculation volume) at  $r = R_{\max}$ . It is in principle possible to take into account the fact that the radius of the pion potential is sensibly smaller than  $R_{\max}$ ; however, we verified that pion spectra from nucleon-induced reactions are insensitive to the potential radius in INCL4.6. Therefore, the refinement seems unwarranted.

Second, the INCL4.6 code introduced a special procedure, named “local  $E$ ” [16], which tries to correct for the unrealistically large momentum content of the nuclear surface in the nuclear model underlying INCL. When a nucleon is involved in a collision, its kinetic energy is

preemptively reduced by an amount that depends on its position (the correction is large at the surface of the nucleus). The nucleon momentum is rescaled accordingly. This procedure tries to capture the fact that nucleons in the surface are close to the turning point of their classical trajectories and, thus, less kinetic energy is available for the collision. The local- $E$  correction is instrumental for the description of nucleon-nucleus reaction cross sections at low incident energy [Section II.C.4.b in 16]. For consistency with nucleon-induced reactions, the same procedure is applied to the nucleon involved in the first collision of pion-nucleus reactions in INCL++. This has some consequences, as we shall illustrate in Section III.

Third, the INCL4.6 code introduced a dependence of the calculation-sphere radius ( $R_{\max}$ ) on the nucleon-nucleon “interaction range” [Section II.D.3 in 16]. In INCL++ the interaction range is taken to be equal to the interaction distance used in the low-energy fusion sector (Eq. (7) below). This is only done for consistency and has no physical consequence.

Finally, target preparation for  $A \leq 4$  is treated differently. The INCL4.6 code singles out this special case and imposes that the sum of the momenta and positions of the target nucleons should vanish, as appropriate for the center-of-mass system; however, these conditions are not conserved during the cascade, even in absence of collisions, due to the presence of the target potential. Moreover, the assumed root-mean-square momenta for these targets are inconsistent with those used when the same nuclei are considered as projectiles. In INCL++, instead, target preparation is consistent for all targets. (Note however that the shape of the momentum distribution is still taken to be different for projectiles and targets, for reasons explained in detail in Section II D.)

Up to the four differences mentioned so far, we can state that INCL++ is physically equivalent to INCL4.6 as far as nucleon- and pion-induced reactions are concerned.

Additional differences specifically concern reactions induced by light nuclei. The value of the “Coulomb radius” (related to the Coulomb barrier, as explained in Ref. 16) for  ${}^3\text{He}$  was found to be inadequate and replaced with the value used for  ${}^4\text{He}$ . This will be illustrated in Section III B. Moreover, polarization of incident deuterons [16, Section II.D.4.d] is neglected in INCL++.

The most important difference between INCL4.6 and INCL++, however, is the ability of the latter to treat reactions induced by light ions, as detailed in Section II B. Note however that the light-ion extension led us to modify the low-energy fusion model even for incident light charged particles ( $A \leq 4$ ), for consistency with the light-ion sector. Therefore, the INCL++ predictions for LCP projectiles at low energy are *not* expected to be in agreement with those made by INCL4.6, as we shall illustrate in Section III below.

The rest of this Section concerns the detailed description of the extension to light-ion projectiles. We start by illustrating the preparation of the projectile nucle-

ons in the laboratory frame (Sections II B 1 and II B 2), which takes into account Coulomb deviation by the target nucleus (Section II B 3). Nucleons entering INC (Section II B 4) are adjusted to allow for excitation energy in the projectile pre-fragment (Section II B 5). The INC phase proper is rather standard and is described in Section II B 6. At the end of INC, a projectile-like pre-fragment is defined if possible (Section II B 7). Reactions at low incident energy require a special treatment and are discussed in Section II C. The limitations of the approach we describe are discussed in Section II D. This completes the discussion of the light-ion extension of INC; however, we also need to discuss the relevance of statistical de-excitation models for the complete simulation of the nucleus-nucleus reaction (Section II E).

## B. Extension to light-ion-induced reactions

It has been demonstrated [18] that the Liège Intranuclear Cascade model can successfully reproduce a vast set of observables pertaining to nucleon-induced reactions between a few tens of MeV and a few GeV, which suggests that the model condenses the physics that is essentially relevant in this energy range. It is therefore natural to take it as a starting point for the development of a new model for light-ion-induced reactions.

The treatment of nucleus-nucleus reactions in an INC framework poses several challenges that do not apply to nucleon-nucleus reactions. First and foremost, there is no natural way of accounting for the binding of the projectile nucleus within the INC scheme. The cascade takes place in a single mean-field potential, which is typically assumed to be that of the target nucleus; this essentially amounts to neglecting the mean-field interaction between the projectile constituents. This approximation might be tenable for central collisions of a light projectile on a heavy target, which rarely lead to the emission of a projectile-like fragment; however, it is clear that no model can describe projectile fragmentation if the binding of the projectile nucleons is neglected. Second, INC models typically do not treat the mean-field potentials as dynamical quantities and assume that they do not evolve during the cascade phase. This is justifiable for nucleon-nucleus reactions, where only a relatively small fraction of the nucleons directly participates in the reaction, but it is clear that pre-fragments produced in nucleus-nucleus reactions can be very different from the initial reaction partners. Therefore, any collective rearrangement of the mean field is beyond the reach of traditional INC models. Third, nucleons in nuclei are endowed with Fermi motion. A realistic description of the intrinsic momentum content of both reaction partners is necessary for an accurate description of certain observables. This is somewhat at odds with the independent-particle Fermi-gas model that is typically used to describe the structure of the reaction partners, especially for light nuclei. The definition of Pauli blocking is unambiguous only if the ini-

Table I. Assumed single-particle space and momentum densities for light projectile nuclei (up to  $A = 18$ ). “MHO” stands for “Modified Harmonic Oscillator” and  $p_F = 270$  MeV/ $c$ . For target nuclei, the same space densities are used; however, hard Fermi spheres are used as momentum distributions [23].

	space, $\rho_p$	momentum, $\pi_p$
deuteron	Paris-potential wavefunction [24]	
$2 < A \leq 6$	Gaussian, RMS from [25]	Gaussian, RMS = $\sqrt{\frac{3}{5}}p_F$
$6 < A \leq 18$	MHO, parameters from [25]	

tial momentum distribution of the nucleons is assumed to be a hard, uniform Fermi sphere. It is well-known however that nucleons in light nuclei exhibit smoother distributions [20], which manifest themselves (among other things) in the momenta of nucleons from the break-up of the projectile. This point will be further developed below (see Sections II D and IV C).

One way to tackle the problem of binding is to separately treat projectile and target nucleons as bound in their respective mean field. This approach is realized e.g. by Isabel [21, 22]. In this model, the reaction dynamics results from the juxtaposition of two conflicting pictures: the nuclei are alternatively depicted as collections of nucleons or as continuous Fermi gases. Nucleons belonging to the projectile or to the target only feel the projectile or the target potential, respectively. Additional assumptions are clearly necessary to determine the dynamics of cascading particles, which do not belong to either nucleus. In this work, we follow an alternative approach.

We briefly repeat here that an INCL-based extension to light-ion-induced reactions has already been attempted [19] on the basis of an old version of the model (INCL4.3). We shall not dwell on the differences between the two approaches here, mostly because the model described in the present work is more sophisticated in several respects and should be considered as the reference point for any future development.

### 1. Preparation of the projectile

The first step in the simulation of a light-ion-induced reaction is the preparation of the projectile and target nuclei. Since the preparation of the target is standard, we refer the reader to Ref. 23 and we limit ourselves to describing the preparation of the projectile in its center-of-mass (CM) frame. Let  $A_p$  and  $Z_p$  be the mass and charge number of the projectile. Furthermore, let  $\rho_p$  and  $\pi_p$  be the single-particle, isospin-independent space and momentum densities of the projectile nucleus. The assumed parametrizations for  $\rho_p$  and  $\pi_p$  are shown in Table I. The table is limited to  $A \leq 18$ , which is the maximum mass that can be treated as a projectile in INCL++. While

this limit is mostly dictated by the needs for applications (reactions involved in carbon-therapy, for instance, rarely involve two nuclei heavier than  $A = 18$ ), it is clear that INC cannot handle the collective behavior of symmetric reactions between heavy nuclei.

In the case of deuteron, projectile preparation is trivial: the relative distance and momentum are independently drawn at random from the Paris space and momentum wavefunction [24]. The directions of the vectors are chosen isotropically. For heavier projectiles, we first draw  $A_p$  isotropically-distributed vectors  $\mathbf{w}_i$  from the space distribution  $\rho_p$ ; let  $\mathbf{W} = A_p^{-1} \sum_i \mathbf{w}_i$  be the mean of the  $\mathbf{w}_i$  vectors; then the positions of the nucleons are defined as

$$\boldsymbol{\rho}_i = \sqrt{\frac{A_p}{A_p - 1}} (\mathbf{w}_i - \mathbf{W}) \quad i = 1, \dots, A_p.$$

By construction, these positions satisfy the relation  $\sum_i \boldsymbol{\rho}_i = 0$ . The scaling factor  $\sqrt{A_p/(A_p - 1)}$  is needed to ensure that the variance of the  $\boldsymbol{\rho}_i$  vectors is equal to the variance of the  $\rho_p$  distribution. The definition of the  $\boldsymbol{\rho}_i$  vectors is such that the first and second central moments of their distribution are equal to the corresponding moments of  $\rho_p$ . In general, the  $\boldsymbol{\rho}_i$  vectors do not strictly follow the  $\rho_p$  distribution, except if the latter is Gaussian; deviations from the shape of  $\rho_p$  are smaller if the number of nucleons is larger.

The CM momenta of the projectile nucleons  $\boldsymbol{\pi}_i$  are constructed in a similar way. Since the momentum distributions are taken to be Gaussian for all projectile nuclei, the generated momenta are normally distributed with the correct width parameter and sum up to zero total momentum, as appropriate for the CM system.

### 2. Projectile binding and Lorentz boost

We choose to account for the projectile binding by putting the nucleons off their mass shell. During the INC phase, it is assumed in INCL that the proton and neutron masses are equal, and they are set to the common value  $m = 938.2796$  MeV [26]. Let  $M_p$  be the mass of the projectile nucleus; we define the *dynamical pseudopotential* of the projectile as

$$V_p = A_p^{-1} \left[ \sum_{i=1}^{A_p} \sqrt{\boldsymbol{\pi}_i^2 + m^2} - M_p \right].$$

This quantity should not be regarded as a physical potential, but rather as a calculation device to enforce the nominal dispersion law in the laboratory frame. The pseudopotential has the dimensions of an energy, is always positive, and is equal to the opposite of the average potential energy that the nucleons would feel if their total relativistic energy were to be equal to the nominal mass of the projectile. Note that  $V_p$  is a random variable because it depends on the values of the drawn nucleon



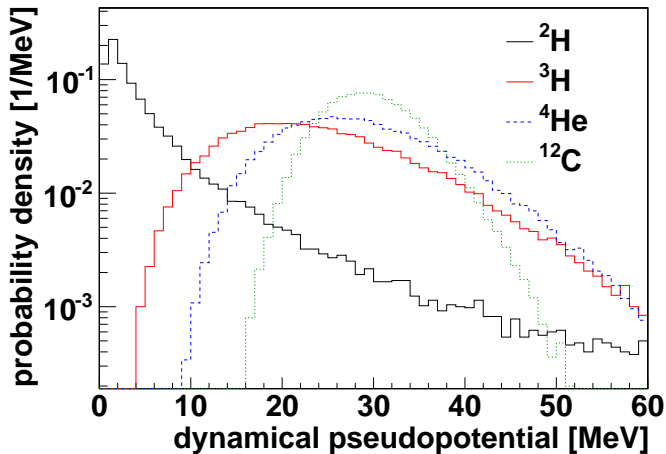


Figure 1. (Color online) Distributions of the dynamical pseudopotential used in the preparation of different light projectiles. Mean values and standard deviations are:  $(8 \pm 18)$  MeV for deuteron,  $(25 \pm 10)$  MeV for triton,  $(29 \pm 9)$  MeV for  ${}^4\text{He}$  and  $(30 \pm 5)$  MeV for  ${}^{12}\text{C}$ .

momenta. Typical distributions for the pseudopotential are shown in Fig. 1. The distribution for deuteron is peculiar because its intrinsic momentum distribution is not assumed to be Gaussian.

We define the nucleon relativistic energies in the center of mass as

$$\varepsilon_i = \sqrt{\boldsymbol{\pi}_i^2 + m^2} - V_p. \quad (1)$$

The four-momenta of the projectile nucleons  $(\varepsilon_i, \boldsymbol{\pi}_i)$  are not on mass shell; however, they satisfy energy- and momentum-balance relations that are appropriate for the center of mass of the projectile, namely:

$$\sum \varepsilon_i = M_p, \quad (2a)$$

$$\sum \boldsymbol{\pi}_i = 0. \quad (2b)$$

Let  $E_p$  indicate the total relativistic energy of the projectile nucleus; assuming that the projectile moves along the positive direction of the  $z$  axis, let  $\mathbf{P}_p = (0, 0, \sqrt{E_p^2 - M_p^2})$  represent its momentum; finally, let  $\gamma = E_p/M_p$ ,  $\beta = \sqrt{1 - 1/\gamma^2}$  and  $\boldsymbol{\beta} = (0, 0, \beta)$  be the nominal Lorentz parameters of the projectile. The four-momenta of the projectile nucleons in the laboratory frame  $(e_i, \mathbf{p}_i)$  are defined by a Lorentz boost on the CM four-momenta:

$$e_i = \gamma(\varepsilon_i + \boldsymbol{\beta} \cdot \boldsymbol{\pi}_i) \quad (3a)$$

$$\mathbf{p}_i = \gamma(\boldsymbol{\pi}_i + \boldsymbol{\beta}\varepsilon_i). \quad (3b)$$

Eqs. (2) guarantee that the energy and momentum balance are correct:

$$\sum e_i = E_p \quad (4a)$$

$$\sum \mathbf{p}_i = \mathbf{P}_p. \quad (4b)$$

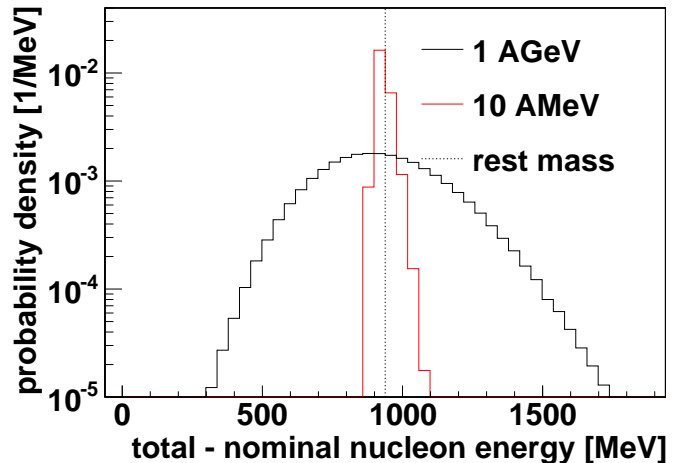


Figure 2. (Color online) Distribution of the total relativistic nucleon energy in the laboratory frame  $e_i$  minus the nominal kinetic energy per nucleon of the projectile, for a  ${}^{12}\text{C}$  nucleus at 1 AGeV (black line) or 10 AGeV (red line).

The positions of the nucleons in the laboratory frame take into account Lorentz contraction along the  $z$  axis.

We illustrate the procedure for the preparation of the nucleons in Fig. 2 with the distributions of nucleon energies for a  ${}^{12}\text{C}$  nucleus at 10 AGeV and 1 AGeV. The nominal kinetic energy per nucleon of the  ${}^{12}\text{C}$  nucleus was subtracted from the total nucleon energy. In absence of Fermi motion, the distributions would collapse to a Dirac delta function centered around the nucleon rest mass.

Note that Fermi motion induces a *larger* spread at 1 AGeV than at 10 AGeV. This is a direct consequence of Eq. (3a) which is easy to visualize for non-relativistic velocities. Indeed, in this limit Eq. (3a) reduces to

$$e_i = m + \frac{\boldsymbol{\pi}_i^2}{2m} + \boldsymbol{\pi}_i \cdot \boldsymbol{\beta} + \frac{m\boldsymbol{\beta}^2}{2}.$$

For fixed absolute values of the boost speed  $|\boldsymbol{\beta}|$  and of the nucleon momentum  $|\boldsymbol{\pi}_i|$ , the fluctuations in  $e_i$  are generated by the only non-constant term on the r.h.s., namely the scalar product  $\boldsymbol{\pi}_i \cdot \boldsymbol{\beta}$ , and are therefore proportional to  $|\boldsymbol{\beta}|$ , i.e. they are more important at high energy than at low energy.

Summarizing, the procedure described above defines positions and four-momenta for the  $A_p$  projectile nucleons in the laboratory frame. The sum of the nucleon four-momenta is equal to the nominal four-momentum of the projectile nucleus. However, the nucleon four-momenta are off mass shell.

Finally, we have also verified that the projectile preparation algorithm is relatively robust with respect to the choice of the reference frame: the nucleon energies are essentially unchanged if we choose to introduce the dynamical pseudopotential in the laboratory frame.

### 3. Coulomb deviation

The projectile preparation step results in the definition of the (off-shell) four-momenta of  $A_p$  nucleons in the laboratory frame. The relative positions of the nucleons in the laboratory frame are also defined. The initial positions of the nucleons with respect to the target nucleus are defined by the impact parameter and by an algorithm that takes into account the Coulomb deviation of the projectile trajectory. The procedure used in INCL++ closely resembles the one used in INCL4.6 [16], to which the reader is referred. The result of the algorithm is to define entrance positions and times for all projectile nucleons into the calculation volume.

The main ingredient is the Coulomb radius  $R_{\text{Coul}}$ , a function of the projectile and target species, which essentially defines the height of the barrier. Compared to the INCL4.6 algorithm, we have a different parametrisation of  $R_{\text{Coul}}$  for  ${}^3\text{He}$  projectiles — we use the same formula for  ${}^3\text{He}$  and  ${}^4\text{He}$ . For projectiles with  $Z > 2$ , which lie outside the scope of the INCL4.6 model, a new prescription has to be given. We choose the following:

$$R_{\text{Coul}} = \frac{e^2 Z_p Z_t}{B_{\text{Shen}}}, \quad (Z_p > 2)$$

where  $Z_t$  is the target charge number and  $B_{\text{Shen}}$  is the Coulomb barrier calculated using Shen's parametrisation [27]:

$$B_{\text{Shen}} = \frac{e^2 Z_p Z_t}{R_p + R_t + 3.2 \text{ fm}} - a \frac{R_p R_t}{R_p + R_t},$$

with  $R_i = (1.12A_i^{1/3} - 0.94A_i^{-1/3}) \text{ fm}$  and  $a = 1 \text{ MeV/fm}$ .

### 4. Geometrical participants, geometrical spectators and dynamical spectators

An important ingredient of the nucleus-nucleus extension is the assumption that projectile nucleons propagate with the (Coulomb-distorted) collective velocity of the projectile beam until they undergo a collision. This has two consequences. First, projectile nucleons can immediately be divided in two classes: those whose trajectory intersects the INCL calculation volume are labeled as *geometrical participants*; the others are called *geometrical spectators*. If there are no geometrical participants, the event is considered as transparent (no reaction). Second, the entrance times of the geometrical participants in the calculation volume can be analytically predicted. The entrance time of the first nucleon is taken as the start of the intranuclear cascade.

It should be stressed that the distinction between geometrical participants and spectators is not physical, because it is a consequence of the finite radius of the INCL calculation volume,  $R_{\text{max}}$ , which is *not* a physical parameter. Ideally, the model predictions (e.g. cross sections) should be completely independent of  $R_{\text{max}}$  (for

sufficiently large values of  $R_{\text{max}}$ ). However, geometrical spectators never enter the calculation volume, and thus cannot undergo any interaction. For continuity, the radius  $R_{\text{max}}$  must be taken sufficiently large so that the probability that a geometrical participant entering close to  $R_{\text{max}}$  undergoes a collision is negligibly small. Still, this condition is not sufficient to ensure that the model predictions are independent of  $R_{\text{max}}$ . Indeed, geometrical participants can traverse the calculation volume without undergoing any collision. Such particles, which we call *dynamical spectators*, must be treated on the same footing as the geometrical spectators. We shall discuss in section II B 7 to what extent this goal has been attained in the current incarnation of INCL++.

### 5. Excitation and kinetic energy of the projectile-like pre-fragment

The intranuclear-cascade phase starts with one of the projectile nucleons entering the calculation volume. This event can actually be seen as the transfer of a nucleon from the projectile to the target nucleus. If we seek to conserve energy during the whole intranuclear-cascade phase, the  $Q$ -value for nucleon transfer must somehow be taken into account in the treatment of the incoming nucleon. In the context of nucleon-induced reactions, this observation has led us to introduce empirical thresholds for particle emission and absorption [16]: the energy of a particle entering and leaving the nucleus is corrected according to differences of masses taken from tables [28]. In nucleus-nucleus reactions, the situation is complicated by the possibility that nucleon transfer from the projectile to the target may leave the projectile in an excited state. The intranuclear-cascade model does not offer any natural prescription to fix the excitation energy of the projectile-like pre-fragment. The reader should contrast this with the excitation energy of the target nucleus, which can be naturally defined as a sum over particle-hole excitations. Therefore, we need to resort to a model to define the excitation energy of the projectile-like pre-fragment.

We postulate that nucleon removal leads to a particle-hole-like excitation energy in the projectile, too. More precisely, assume that only the  $A$  nucleons labeled by  $i = 1, \dots, A$  are left in the projectile; then we define the excitation energy as

$$E_A^* = \sum_{j=1}^A \varepsilon_j - \sum_{j=1}^A \varepsilon_{i_j}. \quad (5a)$$

Here the second summation is intended to run over the  $A$  smallest values of the CM energies  $\varepsilon_i$  (Eq. (1)), which are collectively meant to represent a reference state for the  $A$ -nucleon pre-fragment. The excitation energy is computed as the difference between the total energy left in the pre-fragment CM and the energy of the reference

state. It has the desirable properties of always being non-negative and of vanishing for  $A = A_p$ .

The state of motion of the projectile pre-fragment is also perturbed by nucleon removal. Let  $(E_A, \mathbf{P}_A)$  and  $(E_{A-1}, \mathbf{P}_{A-1})$  be the four-momenta of the pre-fragment before and after nucleon removal,  $A$  being the running mass of the projectile pre-fragment. At the beginning of INC, we have  $A = A_p$ ,  $E_A = E_{A_p} = E_p$  and  $\mathbf{P}_A = \mathbf{P}_{A_p} = \mathbf{P}_p$ . Without lack of generality, we assume that the nucleons are removed from the projectile in decreasing index order (the  $A_p$ -th nucleon first, then the  $(A_p - 1)$ -th, ...). When removing one nucleon, i.e. going from mass  $A$  to mass  $A - 1$ , the change in total momentum is taken equal to minus the momentum (Eq. (3b)) of the removed nucleon:

$$\mathbf{P}_{A-1} = \mathbf{P}_A - \mathbf{p}_A. \quad (5b)$$

The total energy  $E_{A-1}$  is defined by the dispersion relation:

$$E_{A-1} = \sqrt{(M_{A-1} + E_{A-1}^*)^2 + \mathbf{P}_{A-1}^2}, \quad (5c)$$

where  $M_A$  is the tabulated mass of the pre-fragment and the excitation energy  $E_A^*$  is given by Eq. (5a) above. Finally, if there is more than one geometrical participant, the procedure is applied to each nucleon transfer.

## 6. Intranuclear-cascade phase

The excitation energy of the projectile-like pre-fragment, Eq. (5a), was introduced ‘‘by hand’’. If we wish to enforce energy conservation at all steps of the INC, we must compensate for it by correcting the energy of the transferred nucleon. This is necessary even when the excitation energy of the projectile-like pre-fragment does not change, because the nucleon transfer is in general associated with a non-vanishing  $Q$ -value.

It is assumed that the mean field of the target nucleons acts on the projectile nucleon as soon as it enters the calculation volume. Given the total relativistic energy of the projectile nucleon  $e_i$  (Eq. (3a)), we now seek the total relativistic energy  $E_i$  *inside* the target potential. The task is complicated by the fact that the potentials adopted in INCL are not constant but depend on the energy of the nucleon itself, in the spirit of the phenomenology of the optical-potential model [29]. Therefore, the energy  $E_i$  must be sought as a numerical solution to the equation

$$E_i = e_i + V(E_i) + \Delta Q + \Delta E_p^*, \quad (6)$$

where  $\Delta Q$  is a correction due to the difference between the real  $Q$ -value for nucleon transfer and INCL’s internal value, and  $\Delta E_p^*$  is a correction that allows for a change in projectile excitation energy. If the excitation energy of the projectile pre-fragment is unchanged by the nucleon transfer, then  $\Delta E_p^* = 0$ .

As customary, it is assumed in the INC framework that cascading nucleons are on mass shell. Therefore, once the

energy  $E_i$  is determined as the solution of Eq. (6), the magnitude of the nucleon momentum inside the target potential is defined by the on-shell dispersion relation

$$\mathbf{P}_i^2 = E_i^2 - m^2,$$

$m$  being the INCL nucleon mass. The direction of the  $\mathbf{P}_i$  vector is taken to be parallel to  $\mathbf{p}_i$  (Eq. (3b)), the nucleon momentum outside the target potential (i.e. no refraction takes place at the surface).

We draw the attention of the reader to an important detail. As long as the nucleon has not undergone any collision, it is taken to propagate inside the target potential with the *collective* velocity of the projectile nucleus. The intrinsic Fermi motion of the projectile is frozen during propagation. The nucleon four-momentum  $(E_i, \mathbf{P}_i)$  is however correctly used in the computation of the elementary cross sections and in the kinematics of the binary collisions. Once the nucleon has experienced a (non-Pauli-blocked) binary collision, it resumes its normal propagation. Note also that this prescription effectively forbids collisions between projectile nucleons (because their relative distance does not change) until they undergo a collision with a target nucleon.

The intranuclear cascade unfolds normally until another projectile nucleon reaches the surface of the calculation volume. The procedure is then applied to the new nucleon and normal cascade is resumed. Once all the nucleons have entered the calculation volume, the usual conditions for cascade stopping apply [23].

## 7. Definition of the projectile-like pre-fragment

At the end of the intranuclear cascade, a projectile pre-fragment may be defined if some nucleons missed the calculation volume (geometrical spectators) or traversed the calculation volume without undergoing any collision (dynamical spectators). If no dynamical spectators are present, the mass, charge, excitation energy and state of motion of the projectile pre-fragment are already defined (Eqs. (5) above) and are guaranteed to satisfy four-momentum conservation.

However, if dynamical spectators are present and are to be merged back into the projectile-like pre-fragment, some adjustment is necessary to make sure that the resulting pre-fragment is well-defined. Indeed, the non-negativity condition on the excitation energy (Eq. (5a)) is not sufficient because a net energy transfer between the dynamical spectators and the target is always possible because of the application of empirical thresholds for particle absorption/emission.

We then tentatively define the pre-fragment four-momentum as the sum of the four-momenta of the dynamical and geometrical spectators. If the resulting four-momentum leads to a negative excitation energy, we apply an iterative procedure to determine the maximal number of dynamical spectators that can be incorporated

in the pre-fragment without leading to negative excitation energy.

From our discussion it clearly emerges that, despite our efforts, dynamical and geometrical spectators are not (and cannot) be treated on exactly the same footing. The crucial reason for this is that the four-momenta of dynamical spectators are perturbed when they enter the target nucleus. Indeed, their energy is corrected to keep the energy balance satisfied and to possibly make room for some excitation energy of the projectile-like pre-fragment (Eq. (5a)).

### C. Low-energy fusion model

So far we have implicitly assumed that the transfer of one nucleon from the projectile to the target is always possible. However, serious conceptual and technical complications arise if the kinetic energy of one of the entering nucleons is lower than the Fermi energy of the target. One would expect such a process to be forbidden by the Pauli exclusion principle, especially for the first projectile nucleon entering the unperturbed target Fermi sea. This difficulty has already been encountered in the extension of the Fortran version of INCL to light incident clusters [23]. In that case it was observed that the problematic circumstance is most likely to occur when the projectile kinetic energy per nucleon is comparable to or smaller than the dynamical projectile pseudopotential. Under these conditions, it seems reasonable to assume that, independently of the details of the dynamics, most of the incoming nucleons will be trapped by the target potential well, resulting in (possibly incomplete) fusion of the projectile and the target. This argument is especially cogent for reactions between a light composite particle ( $A \leq 4$ ) and a large nucleus. Therefore, for problematic events, INCL4.6 abandons normal INC in favor of a simple geometrical fusion model.

The application of INCL4.6 to low-energy (in the sense outlined above) composite-particle-induced reactions has been proven to produce surprisingly good results [16]. Yet, INCL4.6's fusion model is unsatisfactory inasmuch as only the geometrical participants of the projectile (see section II B 4) are taken to fuse with the target nucleus. The distinction between geometrical participants and spectators has no physical meaning because it is determined by the radius of the calculation volume,  $R_{\max}$ . In INCL4.6, this parameter must be considered as an additional physical ingredient of the model, at least as far as low-energy fusion is concerned.

We were therefore led to revise the low-energy fusion sector in our extension of INCL++ to light incident ions. Admittedly, the fundamental assumption that the low-energy dynamics is dominated by fusion is more difficult to defend for reactions between light ions. This limitation is partly mitigated by the fact that our fusion model naturally yields some "incomplete fusion", as we shall now explain.

The fusion algorithm is triggered if, at any moment during the intranuclear cascade, the particle-entry procedure (section II B 6) endows the entering projectile nucleon with a kinetic energy lower than the target Fermi energy. Normal intranuclear cascade is then abandoned, but the information about the initial position and momenta of the projectile nucleons is retained.

In the spirit of critical-distance fusion models [30, 31], we define an *interaction radius*  $R_{\text{int}}$  and we prescribe that only nucleons whose collective trajectory intersects the sphere of radius  $R_{\text{int}}$  shall fuse with the target nucleus. The interaction radius is defined as

$$R_{\text{int}} = R_0 + d_{\text{int}}$$

in terms of the *interaction distance*  $d_{\text{int}}$ ,

$$d_{\text{int}} = \sqrt{\max(\sigma_{pp}, \sigma_{nn}, \sigma_{pn})/\pi}, \quad (7)$$

where the elementary nucleon-nucleon cross sections  $\sigma_i$  are calculated at the nominal kinetic energy per nucleon of the light-ion projectile.

Nucleons that miss the interaction sphere are assumed not to fuse with the target and are collectively considered as a projectile-like pre-fragment, defined by Eqs. (5). This defines another (possibly excited) source and is expected to mimic incomplete fusion. The four-momentum of the compound nucleus (the source composed of the target and the fusing nucleons) is defined as the difference between the initial total four-momentum and the four-momentum of the projectile-like pre-fragment. If the compound-nucleus four-momentum corresponds to negative excitation energy, the event is discarded and treated as a non-reaction. As a consequence, and in accordance with known phenomenology, incomplete fusion at low projectile kinetic energy is automatically suppressed because energetically forbidden.

The result of the new fusion algorithm is entirely independent of the size of the calculation volume,  $R_{\max}$ ; in this respect, it is more satisfactory than the algorithm used in INCL4.6. However, the condition that triggers the fusion algorithm (energy of the entering nucleon below the Fermi level) is only checked for geometrical participants, and thus still depends on  $R_{\max}$ , although in a much weaker way. One way to avoid this would be to define the shape of the calculation volume in order to suppress the existence of geometrical spectators; this solution would however require a deep revision of the model logic and will not be pursued here.

The differences between INCL4.6's and INCL++'s fusion sectors will be illustrated below (Section III).

### D. Projectile-target asymmetry

The model description above shows that the new nucleus-nucleus capabilities add several new parameter-ingredients to the core of the model. While INCL++'s



treatment of nucleon- and pion-induced reactions can be considered to be essentially parameter-free, the same cannot be said for the nucleus-nucleus sector. The nucleus-nucleus extension is admittedly more phenomenological.

We turn now to a detailed discussion of the limitations of the extended INCL++ model. First and foremost, already at the level of the preparation of the reaction partners, we have to stress that the momentum content of the projectile and the target is different. The momentum distribution of target nuclei is assumed to be a hard Fermi sphere of radius  $p_F = 270 \text{ MeV}/c$  [23], whereas projectile nuclei are assigned a Gaussian distribution with the same RMS momentum ( $\sqrt{3/5} p_F$ ). There are two reasons for this difference. First, only the hard-sphere distribution allows a straightforward definition of Pauli blocking. Even in nucleon-induced reactions, we need to assign a hard-sphere momentum distribution to target nuclei for Pauli blocking to be unambiguously defined. However, hard Fermi spheres are undoubtedly inadequate to describe momentum distributions in light nuclei [20]. Experimental handles on the intrinsic momentum distribution are provided by the momentum distribution of spectator nucleons emitted in peripheral reactions. These observables are better described if realistic momentum distributions are assumed for the projectile nucleus [see e.g. Fig. 22 in Ref. 23]. Thus, our asymmetric choice strikes a compromise between the limitations of the unavoidable Fermi-gas nuclear model and an attempt to improve the quality of the model predictions by the inclusion of known phenomenology.

One of the weaknesses of the light-ion extension here described is that it clearly introduces a projectile-target asymmetry. We can identify a few crucial differences between the treatment of the projectile and of the target:

- the Fermi-momentum distribution is taken to be different for projectiles and targets, as we just discussed;
- the projectile nucleus is essentially treated as a collection of free off-mass-shell nucleons, while the target nucleus is endowed with a mean-field potential;
- Fermi motion in the projectile is frozen, in the sense outlined in Section II B 6;
- projectile nucleons can miss the calculation volume (geometrical spectators, Section II B 4), while target nucleons cannot;
- we neglect Pauli blocking of the first collision in the projectile Fermi sea;
- participant nucleons can escape or finish the reaction in the target-like pre-fragment (they can be trapped by the mean-field potential), but they can never finish in the projectile-like pre-fragment. In the language of the abrasion-ablation picture, the projectile spectator does not receive any energy from the participant zone (final-state interactions);

- the excitation energy assigned to the projectile-like pre-fragment is based on a simple particle-hole model, while that assigned to the target-like pre-fragment results from and carries information about the full INC dynamics;
- the calculation is performed in the target rest frame *and* the dynamics is not Lorentz-covariant because it singles out a global time variable. It has however been shown that the violations introduced by suitable non-covariant dynamics are not necessarily severe, even around 1 AGeV [32]. Note also that there exist no covariant INC models, not even for nucleon- and pion-induced reactions;
- in the low-energy fusion sector, projectile nucleons can elude fusion if their impact parameter is large enough, while target nucleons cannot.

One practical consequence of the projectile-target asymmetry is that the cross sections for producing a given nuclide as a projectile-like fragment or as a target-like fragment will in general not be equal, even for a symmetric reaction (e.g.  $^{12}\text{C}+^{12}\text{C}$ ). Consider however that the predictions for target-like fragment production should be closer to the experimental data, given the superior physical modeling of the target nucleus. This is unfortunate if projectile-like fragmentation is more important than target-like fragmentation for a specific application. However, if both reaction partners are light, one can consider swapping the roles of projectile and target in the simulation: in other words, the reaction can be simulated in inverse kinematics (i.e. as target on projectile), with the reaction products being boosted back to the laboratory frame at the end of the simulation. We refer to this calculation method as *accurate-projectile mode*, while we use the expression *accurate-target mode* to refer to the normal INCL++ calculation mode. The naming convention reflects our expectations about the accuracy of the predictions for projectile- and target-like fragments, which are kinematically well separated. However, the statement about the calculation accuracy should be tempered for lighter particles, and nucleons in particular, whose origin cannot be clearly discriminated on a kinematical basis. We shall illustrate the differences between the two calculation modes in Section IV.

We should stress that the choice between accurate-target and accurate-projectile mode is application-dependent. If the user is interested e.g. in projectile-like fragments for radiation-protection and hadrontherapy simulations, they should use accurate-projectile mode. A universal choice is not possible; however, we believe that accurate-projectile mode provides a better description of particle transport for several applications where INCL++ is likely to give accurate results. Therefore, Geant4 uses INCL++ in accurate-projectile mode by default. The Geant4 user can switch to accurate-target mode using a macro.

The accurate-projectile/target option should be contrasted with the approach used by many INC models

Table II. Choices for the internal reaction kinematics in INCL++ for nucleon- and nucleus-nucleus reactions, when the model is used within Geant4;  $A_p$  and  $A_t$  represent the projectile and target mass numbers within particle transport. The table entry indicates which nucleus is internally treated as the projectile in INCL++. Note that reactions with  $A_p > 18$  and  $A_t > 18$  are delegated to BIC.

	accurate- projectile mode	accurate- target mode
$A_p < A_t \leq 4$	projectile	projectile
$A_t \leq A_p \leq 4$	target	target
$A_p \leq 4 < A_t$	projectile	projectile
$A_t \leq 4 < A_p$	target	target
$4 \leq A_p \leq 18$ and $4 \leq A_t \leq 18$	target	projectile
$A_p \leq 18 < A_t$	projectile	projectile
$A_t \leq 18 < A_p$	target	target

(including Geant4’s BIC model) when treating composite projectiles, in which one identifies the lighter nucleus with the projectile and the heavier nucleus with the target of the INC. The rationale behind the “light-on-heavy” criterion is that the largest nucleus is expected to dominate the mean-field potential. However, this paradigm does not provide clear guidelines for symmetric reactions; furthermore, even in quasi-symmetric reactions (e.g.  $^{12}\text{C}+^{16}\text{O}$ ), one can hardly expect the mean field to be dominated by the heavier partner. Therefore, it seems unwarranted to systematically select the light-on-heavy option, especially if reactions between light nuclei (such as those encountered in hadrontherapy) are involved. Nevertheless, it is probably reasonable to always treat the lightest nuclei as projectiles. Therefore, INCL++ in Geant4 runs calculations as light-on-heavy if either reaction partner has  $A \leq 4$ , regardless of the calculation mode chosen by the Geant4 user. The light-on-heavy mode is also selected if either reaction partner is a heavy nucleus ( $A > 18$ ). The choices for the reaction kinematics are summarized in Table II. In summary, the user-specified accurate-projectile/target option is honored only if both projectile and target masses satisfy  $4 \leq A \leq 18$ .

As an alternative to the accurate-projectile/target dichotomy, it would be possible to palliate the model asymmetry by randomly choosing to simulate the reaction in the rest frame of the projectile or of the target. It is fair to assume that symmetric reactions should result in a straightforward 50-50 split between the two kinematical choices; it is however unclear what should be done of asymmetric reactions such as  $^{12}\text{C}+^{16}\text{O}$ , especially because reactions induced by  $A \leq 4$  projectiles should always be described as light-on-heavy and the model should behave continuously as a function of the projectile mass. Therefore, additional prescriptions would be necessary in this case. Nevertheless, we shall illustrate random sym-

metrization in Section IV with a few selected examples for symmetric reactions.

### E. De-excitation stage

Before turning to the comparison of the new INCL++ model results with nucleus-nucleus experimental data, we need to spend a few words about the coupling with de-excitation models. Historically, the INCL model has been coupled to statistical evaporation/fission models such as ABLA V3 [33] or ABLA07 [17]. This was motivated by the typical application of INCL to spallation reactions, and in particular to reactions induced by nucleons on relatively large nuclei ( $A \gtrsim 50$ ); for these systems, the excitation energy is relatively low and evaporation/fission models are indeed capable of providing a very good description of most observables [18]. It is legitimate to ask whether these models would perform equally well on reactions between light nuclei.

One peculiarity of such reactions is that the binding energy and the excitation energy of the remnants produced by the INC stage may be of the same order of magnitude. Under these conditions, de-excitation becomes a relatively fast process and it is questionable to make use of the statistical hypothesis, or at the very least it seems inappropriate to describe the de-excitation step as a well-defined sequence of binary, evaporation-like splits. This issue is even more pressing as the sensitivity of the model predictions to the details of de-excitation in general increases with the excitation energy.

An alternative picture is provided by Fermi break-up (FBU), a model that was initially developed to describe the production of pions in high-energy nucleon-nucleon collisions [34] and that was subsequently adapted to the description of fragmentation of excited light nuclei [35]. The model does not provide a time-like description of the de-excitation chain, but limits itself to providing probabilities for the final configurations, which are specified by the masses, charges and momenta of the observed cold fragments. The crucial assumption of the model is that the probability to observe a given fragment configuration is simply proportional to the density of phase-space states around it. This amounts to assuming that the transitions from the excited pre-fragment to all the final configurations are described by the same matrix elements; in this sense, the Fermi model represents the simplest possible description of simultaneous nuclear break-up. More sophisticated approaches are provided by the family of statistical multifragmentation models, which will not be discussed here; we refer the reader to Ref. 36 for an account of the relations that the two model classes bear to each other.

The default Geant4 de-excitation model [G4ExcitationHandler, 37] implements FBU as one of the possible channels. However, standard FBU does not provide absolute decay widths, but only yields probabilities for each break-up configuration; for this reason,

it is non-trivial to introduce direct competition between FBU and other de-excitation mechanisms, such as particle evaporation. The developers of G4ExcitationHandler made the choice of applying FBU for any de-exciting nucleus with  $A \leq 16$  and  $Z \leq 8$ ; note that the choice for the threshold values can affect the calculated cross sections by as much as a factor of two [38]. The FBU mechanism can also be triggered during the de-excitation chain, if particle evaporation or other mechanisms bring the excited nucleus in the  $A$ - $Z$  region indicated above.

In what follows (Sections III and IV) we shall compare the results of calculations performed with INCL++ coupled with ABLA07, ABLA V3 and G4ExcitationHandler. Although the ABLA07 model does not include a FBU module, it does include a semi-empirical treatment of multifragmentation [17]. We will discuss below to what extent this makes it applicable to the highest excitation energies. Also, we draw the reader's attention to the fact that ABLA07 is not available for transport calculations in the official Geant4 code; a C++/Fortran interface to ABLA07 can however be privately provided on request. The INCL4.6/ABLA07 code has been included in a private version of MCNPX and is expected to be distributed with a future release of the MCNP6 code [39]; that version is however incapable of handling light-ion-induced reactions.

### III. COMPARISON WITH INCL4.6

We shall now document the physical equivalence of the INCL4.6 and INCL++ codes. Figure 3 shows double-differential cross sections for the production of positive pions from a 730-MeV proton colliding with a copper target; this observable is entirely due to the intranuclear-cascade stage of the reaction. Figure 4 shows double-differential cross sections for the production of neutrons from a 800-MeV proton colliding with a lead target. Finally, Fig. 5 shows the mass distribution of the fragments produced in a 1-GeV  $^{208}\text{Pb}+^1\text{H}$  reaction. The observables depicted in Figs. 4 and 5 are also sensitive to the de-excitation stage of the nuclear reaction. Specifically, de-excitation dominates the low-energy part of the double-differential neutron spectrum (say up to 20 MeV) and is entirely responsible for the mass distribution of Fig. 5, albeit the production of residues with the largest masses is dominated by INC. For the purpose of these comparisons, we coupled our cascade models with the ABLA07 de-excitation model [17]. All plots show perfect agreement between INCL4.6 and INCL++.

We also show calculations performed by coupling INCL++ with the G4ExcitationHandler and ABLA V3 de-excitation models, available in Geant4. De-excitation is the dominant mechanism for the production of the low-energy neutrons in Fig. 4; one indeed remarks that the G4ExcitationHandler yields around 1 MeV are intermediate between those predicted by ABLA V3 (lowest) and ABLA07 (highest). There is a difference of about a factor

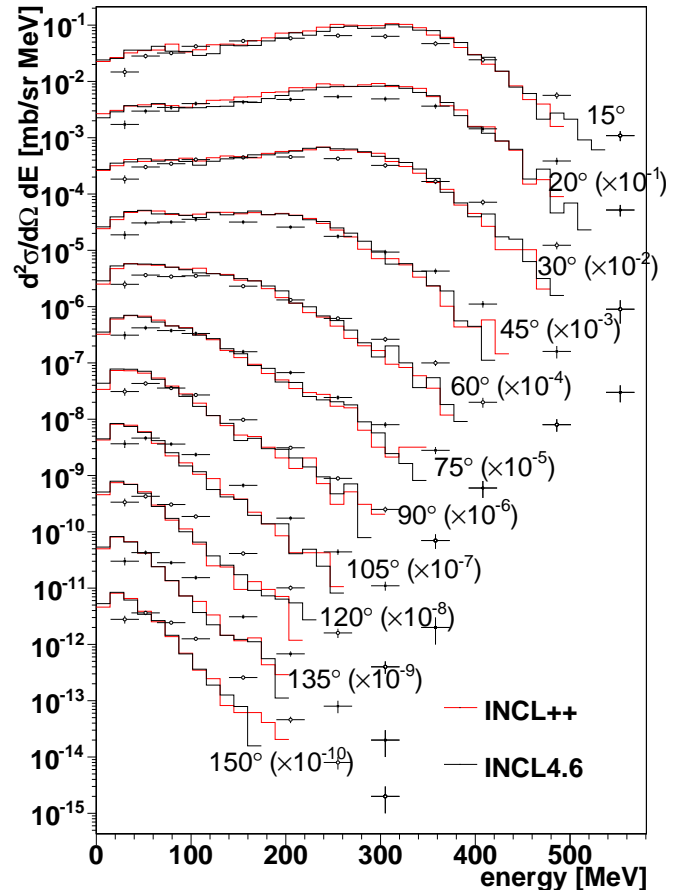


Figure 3. (Color online) Double-differential cross section for  $\pi^+$  production from the 730-MeV  $p+\text{Cu}$  reaction. Red (black) lines represent the INCL++ (INCL4.6) result. Data taken from Ref. 40.

of 2 between ABLA V3 and ABLA07, with the latter being closer to the experimental data. Note however that ABLA V3 also results in larger yields around 10 MeV, which seems to improve the agreement with the experimental data in that region. This difference probably indicates the average kinetic energy of the emitted neutron is higher in ABLA V3 than in ABLA07.

Figure 5 provides a somewhat complementary picture for a similar system. Although ABLA V3 and ABLA07 predict rather different neutron yields, this seems to have little impact on the fission cross section. However, ABLA07's fission sector is substantially different from ABLA V3's model and was probably readjusted to fit the data shown here. INCL++/G4ExcitationHandler largely overpredicts the fission cross section and underestimates the yields for heavy spallation residues ( $A \simeq 175$ ). Note however that the parameters of G4ExcitationHandler were tuned to yield a correct reproduction of the data in Fig. 5 when coupled with BIC [37].

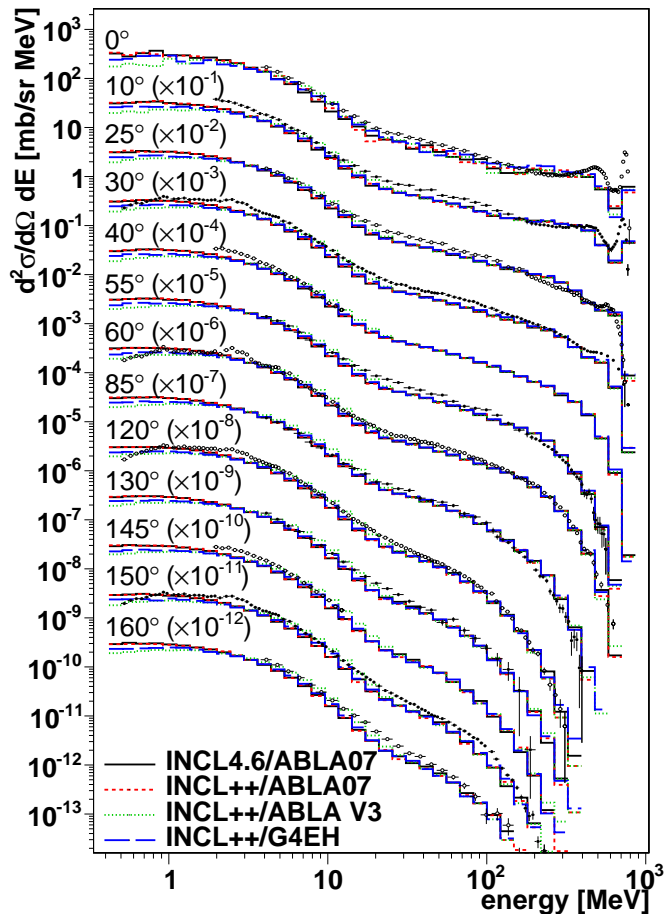


Figure 4. (Color online) Double-differential cross section for neutron production from the 800-MeV  $p$ +Pb reaction. The different model calculations are described in the text ( $G4EH$  in the plot legend stands for G4ExcitationHandler). Data taken from Refs. 41, 42.

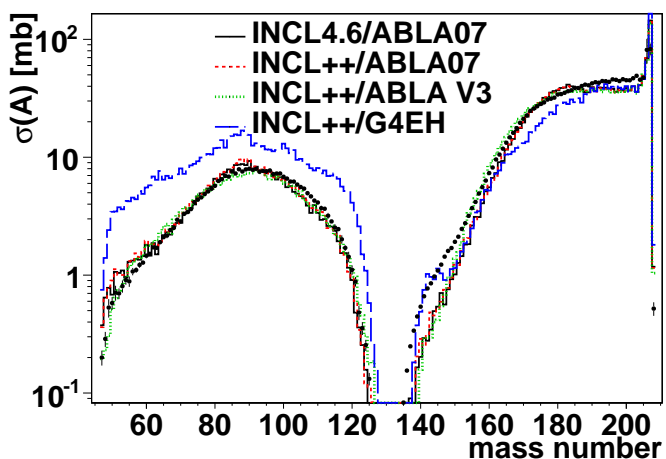


Figure 5. (Color online) Fragmentation cross sections for the 1-A GeV  $^{208}\text{Pb}+^1\text{H}$  reaction, as a function of the fragment mass number. The different model calculations are described in the text ( $G4EH$  in the plot legend stands for G4ExcitationHandler). Data taken from Refs. 43 and 44.

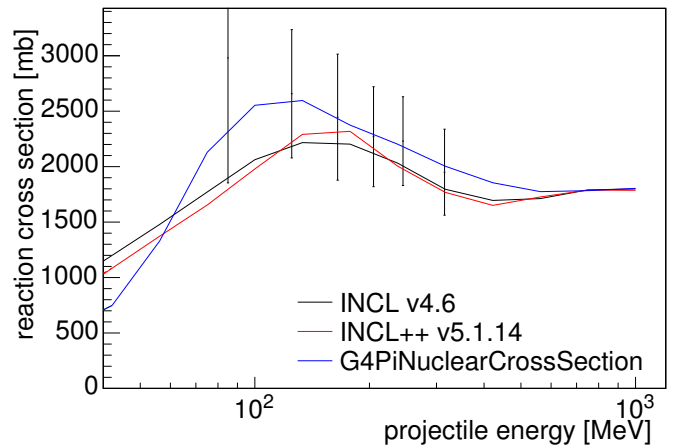


Figure 6. (Color online) Excitation function for the  $\pi^+ + ^{209}\text{Bi}$  reaction cross section, calculated with INCL++ (red line), INCL4.6 (black line) and Geant4's semi-empirical reaction-cross-section model (blue line). Experimental data taken from Ref. 45.

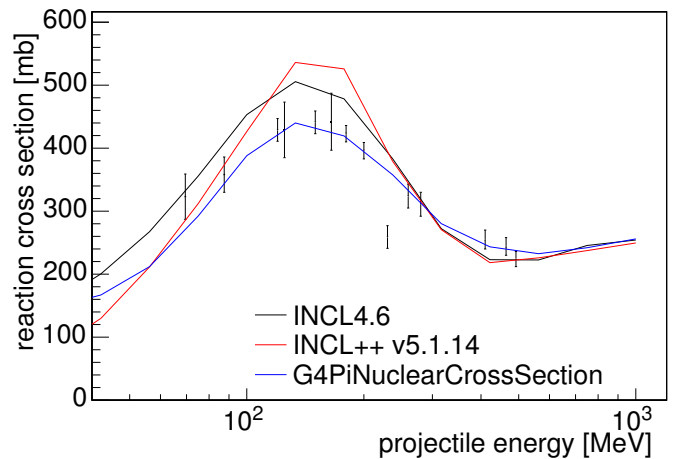


Figure 7. (Color online) Same as Fig. 6, for  $\pi^- + ^{12}\text{C}$ . Experimental data taken from Refs. 45–48.

### A. Reactions induced by pions

As mentioned in Section II A, INCL4.6 and INCL++ mainly diverge in the treatment of reactions induced by pions and composite particles. The most prominent difference in pion-induced reactions is the application of the local- $E$  correction on the first pion-nucleon collision. The net effect of the correction is to reduce the center-of-mass energy at which the pion-nucleon collision takes place. We can reasonably expect this to have an effect on the pion-nucleus reaction cross section, inasmuch as the latter tracks the energy dependence of the elementary pion-nucleon cross section. A similar argument explains the effect of the local- $E$  correction on nucleon-nucleus reaction cross sections [Section III.B in 16].

The effect of the local- $E$  correction on pion-nucleus reaction cross sections is illustrated in Figs. 6 and 7.



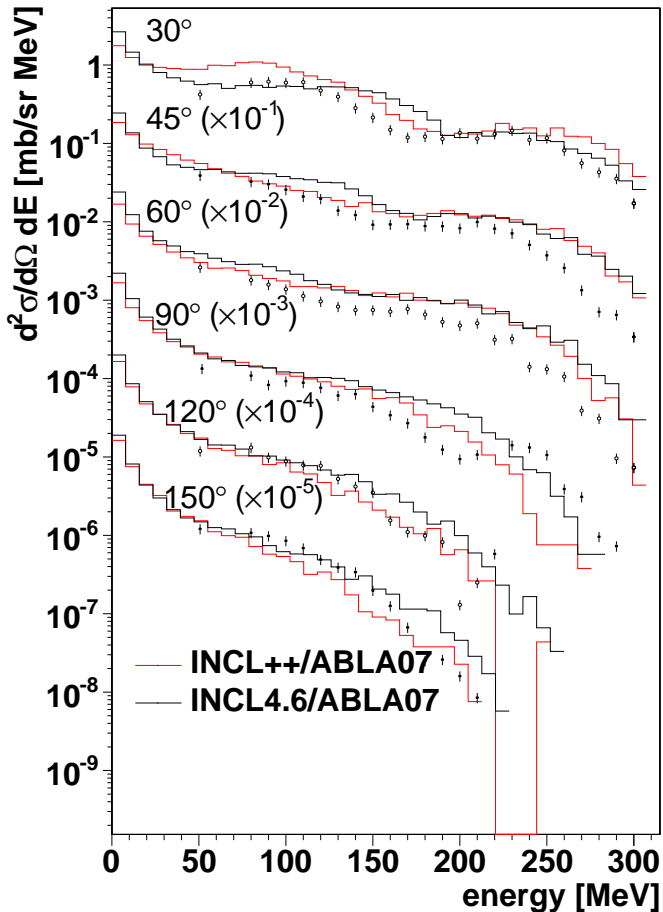


Figure 8. (Color online) Double-differential cross section for proton emission in 220-MeV  $\pi^+ + {}^{12}\text{C}$ , calculated with INCL++ (red line) and INCL4.6 (black line). Experimental data taken from Refs. 49.

The reaction cross section used by the Geant4 particle transport is also shown for comparison. The difference is mostly visible at low energy, which is the region where the elementary pion-nucleon reactions varies most quickly due to the presence of the  $\Delta(1232)$  resonance, but it stays very small in all cases. Note that the calculations in Fig. 7 were performed with INCL++ v5.1.14, corrected for a small bug in the Coulomb deviation of incoming negative particles. The bug is fixed in Geant4 v10.0.p03 and v10.1 $\beta$ .

Note that the reaction cross sections calculated by INCL++ are *not* used for particle transport in Geant4. The transport algorithm relies on independent, semi-empirical cross-section parametrisations, which are generally more accurate than the cross sections predicted by the nuclear-reaction models. (This remark also applies to the nucleus-nucleus reaction cross sections depicted below, in Figs. 10, 11 and 13.) An unreasonable prediction for the reaction cross section is however a sign that some physics is not suitably accounted for.

The local- $E$  correction for pion-induced reactions also manifests itself in other observables, such as double-

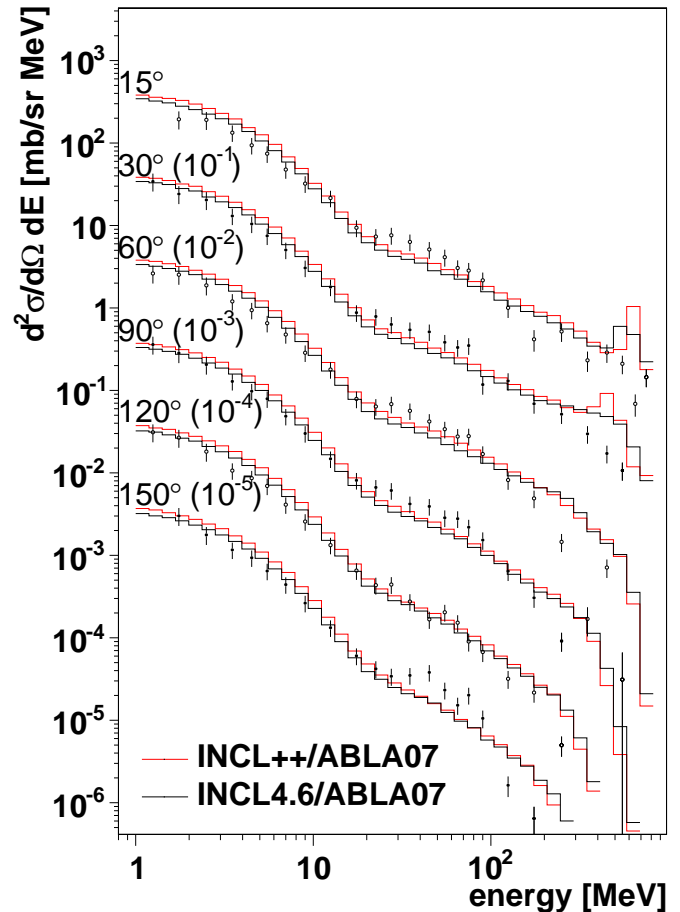
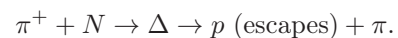
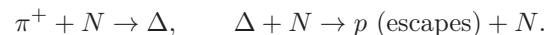


Figure 9. (Color online) Double-differential cross section for neutron emission in 870-MeV  $\pi^- + {}^{208}\text{Pb}$ , calculated with INCL++ (red line) and INCL4.6 (black line). Experimental data taken from Refs. 50.

differential cross sections for proton (Figs. 8) and neutron emission (Fig. 9). The 220-MeV experimental data show some peculiar structure at forward angles that is typical of pion absorption. At  $30^\circ$  one can distinguish two humps centered around 110 and 230 MeV. The 110-MeV peak corresponds to the emission of a proton by intermediate excitation and decay of a  $\Delta$  resonance [51]:



The 230-MeV peak corresponds instead to the absorption of the intermediate resonance:



It is clear that the second mechanism leads to higher proton kinetic energies (on average) because of the absorption of the pion mass.

The energy distributions for these components are smeared out by the Fermi motion of the nucleons in the target. Since the local- $E$  correction suppresses the importance of Fermi motion in the nuclear surface, we observe that the peaks are somewhat sharper

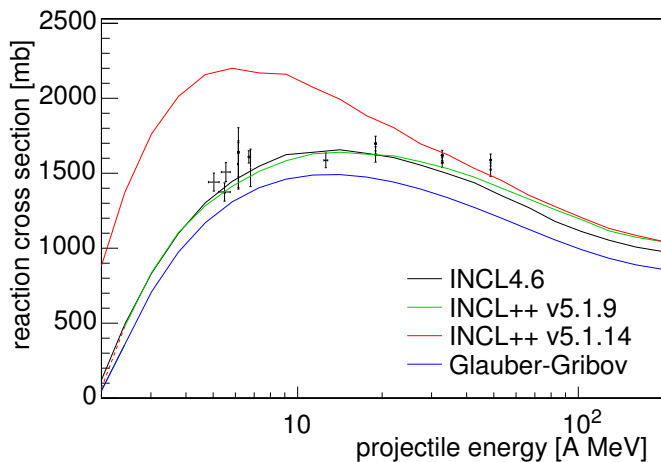


Figure 10. (Color online) Excitation function for the  $d+^{56}\text{Fe}$  reaction cross section, calculated with two versions of INCL++ (red and green lines), INCL4.6 (black line) and Geant4's Glauber-Gribov semi-empirical reaction-cross-section model (blue line). Experimental data refer to  $^{56-58}\text{Fe}$  and  $^{58-60}\text{Ni}$  targets and are taken from Refs. 52–55.

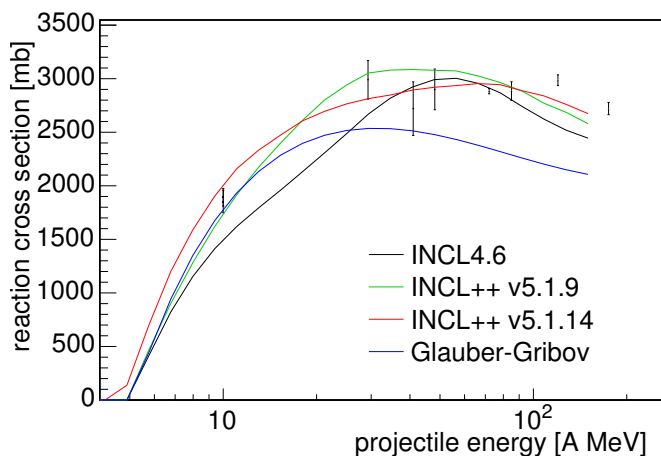


Figure 11. (Color online) Excitation function for the  $^4\text{He}+^{208}\text{Pb}/^{209}\text{Bi}$  reaction cross section, calculated with two versions of INCL++ (red and green lines), INCL4.6 (black line) and Geant4's Glauber-Gribov semi-empirical reaction-cross-section model (blue line). Experimental data refer to  $^{208}\text{Pb}$  and  $^{209}\text{Bi}$  targets and are taken from Refs. 56–58.

in the INCL++ calculations. A similar consideration can be made concerning Fig. 9, where one observes that INCL++ leads to a sharper peak around 600 MeV, which is less satisfactory.

## B. Reactions induced by light composite particles

We mentioned in Section IIA that INCL++ and INCL4.6 differ in how they handle composite projectiles, especially at low energy. This is illustrated by Figs. 10 and 11, which show a comparison of the predicted reaction cross section for the  $d + ^{56-58}\text{Fe}/^{58-60}\text{Ni}$

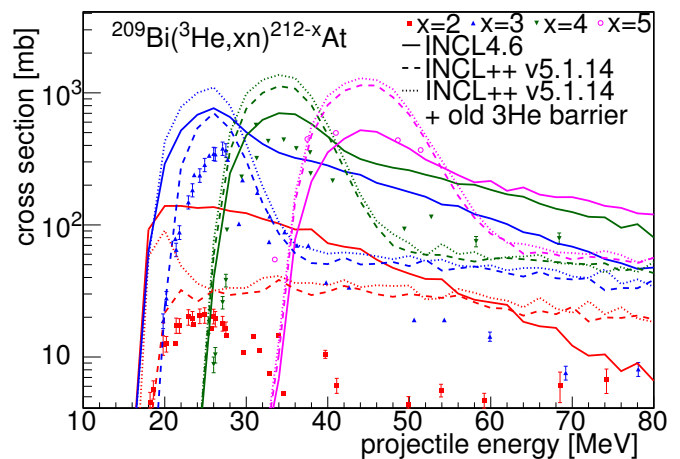


Figure 12. (Color online) Excitation functions for  $^{209}\text{Bi}(^3\text{He},xn)^{212-x}\text{At}$  cross sections. Different colors refer to different values of  $x$ , while the line styles denote calculations performed with INCL4.6 (solid), INCL++ v5.1.14 (dashed) and INCL++ v5.1.14 with the  $^3\text{He}$  Coulomb radius as in INCL4.6 (dotted). Data taken from Refs. 59–61.

and  $^4\text{He}+^{208}\text{Pb}/^{209}\text{Bi}$  system. INCL++ performs sensibly worse than INCL4.6 for the deuteron-induced reaction, while predictions for  $^4\text{He}$  are similar. The degradation is essentially due to the fact that INCL++ uses a unique parameter set to describe reactions induced by composite particles up to  $A = 18$ , while INCL4.6 was limited to  $A \leq 4$ .

Figures 10 and 11 also show the predictions of INCL++ v5.1.9 (green lines), which is the version that was distributed with Geant4 v9.6.p02. The similarity to the INCL4.6 results is due to the fact that the two models have very similar low-energy fusion sectors. We will show in Section IV that INCL++ v5.1.9 is unsuitable for light-ion-induced reactions.

Another difference between INCL4.6 and INCL++ is illustrated by Fig. 12, which shows excitation functions for the  $^{209}\text{Bi}(^3\text{He},xn)$  reactions. As for Figs. 10 and 11, the projectile energies are rather low and we mostly probe the fusion sector of the INCL model; this is why the INCL4.6 and INCL++ calculations are in disagreement. However, Fig. 12 also illustrates the effect of the modification of the Coulomb barrier for incoming  $^3\text{He}$  nuclei. The calculations for INCL++ v5.1.14 are in better agreement with the experimental data than the modified calculations with the old Coulomb barrier, and even than the calculations performed with the legacy INCL4.6 model.

## IV. COMPARISON WITH NUCLEUS-NUCLEUS EXPERIMENTAL DATA

We now turn to the verification of the most prominent new feature of INCL++, namely the capability to handle light-ion-induced reactions. The observables selected

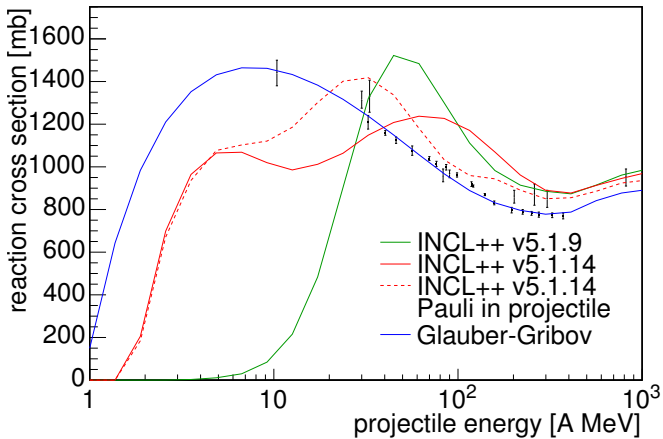


Figure 13. (Color online) Excitation function for the  $^{12}\text{C}+^{12}\text{C}$  reaction cross section, calculated with INCL++ v5.1.9 (green line), INCL++ v5.1.14 (solid red line), INCL++ v5.1.14 with Pauli blocking and a hard Fermi sphere in the projectile (dashed red line) and Geant4’s Glauber-Gribov semi-empirical reaction-cross-section model (blue line). Experimental data taken from Refs. 69–74.

for verification reproduce the choices made for nucleon-nucleus reactions [16, 23], a strategy that proved successful [18]. We start by considering reaction cross sections, which capture global aspects of the model (Section IV A). We will then proceed to investigate double-differential cross sections for the production of nucleons and LCPs (Section IV C). The rationale for this choice lies in the fact that particle emission during INC proceeds more or less directly from hard nucleon-nucleon scattering events, which constitute the core of the cascade mechanism. In certain kinematical regions, de-excitation of the pre-fragments contributes to (or dominates) particle production; therefore, double-differential cross sections indirectly verify some global characteristics of the cascade pre-fragments, too.

Finer details about the distribution of cascade pre-fragments are emphasized by fragmentation cross sections (Section IV E), especially if per-isotope information is available. Although it may be non-trivial to disentangle the contributions of cascade and de-excitation, the study of isotopic fragmentation cross sections for different systems and energies has proven extremely valuable in the development of the proton-nucleus model [16, 23].

We remark in passing that most of the experimental data were analyzed with other models; see for example the vast validation effort of the MCNPX/MCNP6 event generators CEM and LAQGSM [62–68]. We will however not enter into a detailed comparison because these calculations have no direct bearing upon Geant4.

### A. Reaction cross sections

Figure 13 shows an excitation function for the  $^{12}\text{C}+^{12}\text{C}$  reaction cross section. The agreement with the exper-

imental data is far from perfect. More precisely, we can observe that the double-humped INCL++ excitation function clearly exhibits two distinct regimes. The low-energy peak (around 5 A MeV) is due to the fusion model. In fact, pure INC plays essentially no role as long as at least one projectile nucleon enters the calculation volume below the Fermi energy. The importance of the fusion mechanism starts to decrease above 5 A MeV and gradually leaves room for the pure INC mechanism, which is responsible for the second peak (around 70 A MeV).

Particle transport in Geant4 is not seriously affected by this deficiency, because the reaction cross section is imposed during the transport step; however, the disagreement clearly indicates a failure to correctly describe the physics of this reaction, especially at low energy. It might be argued that the  $^{12}\text{C}+^{12}\text{C}$  reaction does not represent a fair benchmark for intranuclear-cascade models, which assume that the larger reaction partner is left relatively unperturbed by the cascade; however, the reaction cross section is determined by the *first* non-Pauli-blocked nucleon-nucleon collision, which typically involves surface nucleons at an early, relatively unperturbed stage of the reaction.

In spite of the disappointing result of Fig. 13, the comparison with the double-differential and residue-production data (Sections IV C and IV E below) shows that INCL++ in general captures the essential aspects of the fragmentation in the  $^{12}\text{C}+^{12}\text{C}$  reaction.

Note that the INC approximation is expected to be valid above some 150 A MeV. In this energy range, the contribution from the (admittedly empirical) fusion sector is negligible, thereby simplifying the interpretation of the resulting cross section. We see that the model overestimates the experimental data by about 25%; part of the overestimation is due to the fact that we neglect strict Pauli blocking of the first collision in the Fermi sea of the projectile. This analysis is corroborated by the observation that the nucleon- $^{12}\text{C}$  reaction cross sections are correctly predicted in the same energy-per-nucleon range [16]. As mentioned in Section II D, the use of realistic (Gaussian) momentum distributions for the projectile is somewhat irreconcilable with the definition of Pauli blocking. We therefore performed a test calculation with a hard Fermi sphere for the projectile momentum distribution; strict Pauli blocking in the projectile Fermi sea was applied on the first collision. The resulting excitation function is displayed in Fig. 13 and is in much better agreement with the experimental data. Note also that the refined calculations yields a *larger* reaction cross section between  $\sim 5$  and  $\sim 60$  A MeV; this is an effect of the hard Fermi sphere and is of course not due to the introduction of Pauli blocking.

Finally, Fig. 13 also shows the prediction of an older version of INCL++ (v5.1.9). As mentioned above, the interest of this comparison mainly lies in the fact that the low-energy fusion sector of v5.1.9 is a straightforward extension to  $A \leq 18$  of the INCL4.6 approach. The reaction cross section at low energy (say below 10 A MeV)

is largely suppressed because almost all impact parameters result in incomplete fusion, which is energetically forbidden by the tight binding of  $^{12}\text{C}$  nuclei. It is apparent that INCL++ v5.1.9 is inadequate, which justifies the revision of INCL++'s low-energy sector that was described in Section II C.

### B. Caveat about cross-section normalization

Before turning to double-differential cross sections for particle production, a word of caution should be said about the comparisons shown in the following sections between INCL++ and the other models available in Geant4. As already mentioned above (Section III A), most nuclear-reaction models are able to predict absolute reaction cross sections; however, these quantities are not directly used in particle transport, because more accurate semi-empirical parametrizations are usually available. Nevertheless, a misprediction of the reaction cross section might indicate that the model fails to describe some particular channel. We try to make our point clearer by referring to Fig. 13 above. We showed that the overprediction of the  $^{12}\text{C}+^{12}\text{C}$  reaction cross section at high energy is largely due to the lack of Pauli blocking on the first collision in the projectile Fermi sea. This defect should mostly lead to an overestimation of the cross sections associated with peripheral collisions. Therefore, even though the gross overestimation is only 25% of the reaction cross section, the relative overprediction may be much more conspicuous in channels associated with peripheral collisions.

The Geant4 nuclear-reaction models discussed below (QMD, BIC, Bertini+PreCompound) are only accessible through their Geant4 interface classes. Because of the way nuclear-reaction models are used in particle transport, the interface iterates calls to the model engine until an inelastic event is generated. Therefore, the absolute reaction cross sections predicted by the Geant4 models are *not* available to us. We chose to normalize the raw model predictions (counts) using the Shen nucleus-nucleus cross section [27], which is available in Geant4 through class G4IonsShenCrossSection.

### C. Particle-production cross sections

Figure 14 demonstrates the difference between accurate-projectile and accurate-target mode (see Section II D) using double-differential cross sections for neutron production from the symmetric 290-AMeV  $^{12}\text{C}+\text{C}$  [75] reaction. Note that the incident energy is large enough so that the low-energy fusion sector can be neglected. Both calculations were coupled to the native Geant4 de-excitation model [37]. Differences are mostly visible at forward angles and low energy; the predictions for the largest angles are very close to each other. In general, the shapes of the experimental spectra are quite

well reproduced by both INCL++ calculations. Therefore, we conclude that neutron emission is nevertheless projectile-target symmetric to a good degree.

Note that the experimental data show a peak at forward angles roughly centered around the nominal energy per nucleon of the projectile and corresponding to neutrons with a rather small energy in the projectile rest frame. In INCL++, they mainly originate from the break-up of the projectile nucleus. The shape and the height of the peak depend on the selected de-excitation model; this is illustrated again by Fig. 14, where the accurate-projectile calculation coupled with G4ExcitationHandler (which for this system reduces to Fermi break-up, see Section II E) is contrasted to an INCL++/ABLA V3 calculation (solid and dashed red lines, respectively). The ABLA V3 model yields a larger peak, in better agreement with the experimental data at forward angles, but also affects the low-energy neutron yields.

The shape of the projectile-fragmentation peak is also sensitive to the assumed Fermi momentum of the projectile nucleus. This is illustrated by an accurate-projectile INCL++ calculation using a mass-dependent Fermi momentum given by

$$\begin{aligned} p_F(A) &= \alpha - \beta \exp(-\gamma A) \\ \alpha &= 259.416 \text{ MeV}/c \\ \beta &= 152.824 \text{ MeV}/c \\ \gamma &= 9.5157 \cdot 10^{-2}. \end{aligned}$$

This formula is a fit to Moniz et al.'s direct measurements by quasi-elastic electron scattering [76]. For  $^{12}\text{C}$ , the formula yields  $p_F(^{12}\text{C}) \simeq 210 \text{ MeV}/c$  (Moniz et al.'s measurement is actually  $(221 \pm 5) \text{ MeV}/c$ ), which is not very different from the default INCL++ value of  $270 \text{ MeV}/c$  (see Table I). Nevertheless, Fig. 14 shows that the neutron spectra are roughly equally sensitive to the de-excitation model and to the Fermi momentum.

The sensitivity to  $p_F$  can be enhanced by looking at lighter projectiles, such as  $^4\text{He}$  in the 230-AMeV  $^4\text{He}+\text{Cu}$  reaction depicted in Fig. 15. Here  $p_F(^4\text{He}) = 155 \text{ MeV}/c$ , almost a factor of two smaller than the nominal INCL++ value. For this system, standard INCL++ fails to describe the part of the spectrum above 200 MeV. However, the projectile-fragmentation peak at forward angles is much better reproduced using the empirical Fermi momentum. Nevertheless, since we have not extensively tested the implications of empirical Fermi momenta in INCL++, we keep  $p_F = 270 \text{ MeV}/c$  as the default value. We reserve a detailed study to a future publication.

Figures 14 and 15 suggest that INCL++ generally succeeds to capture the essential aspects of the experimental data. This conclusion is corroborated by Figures 16 and 17, which show a comparison of the INCL++ result (in accurate-projectile mode) to calculations performed by other models available in Geant4: QMD model (blue), BIC [79] (green) and Bertini+PreCompound [80–82] (cyan, only applicable for



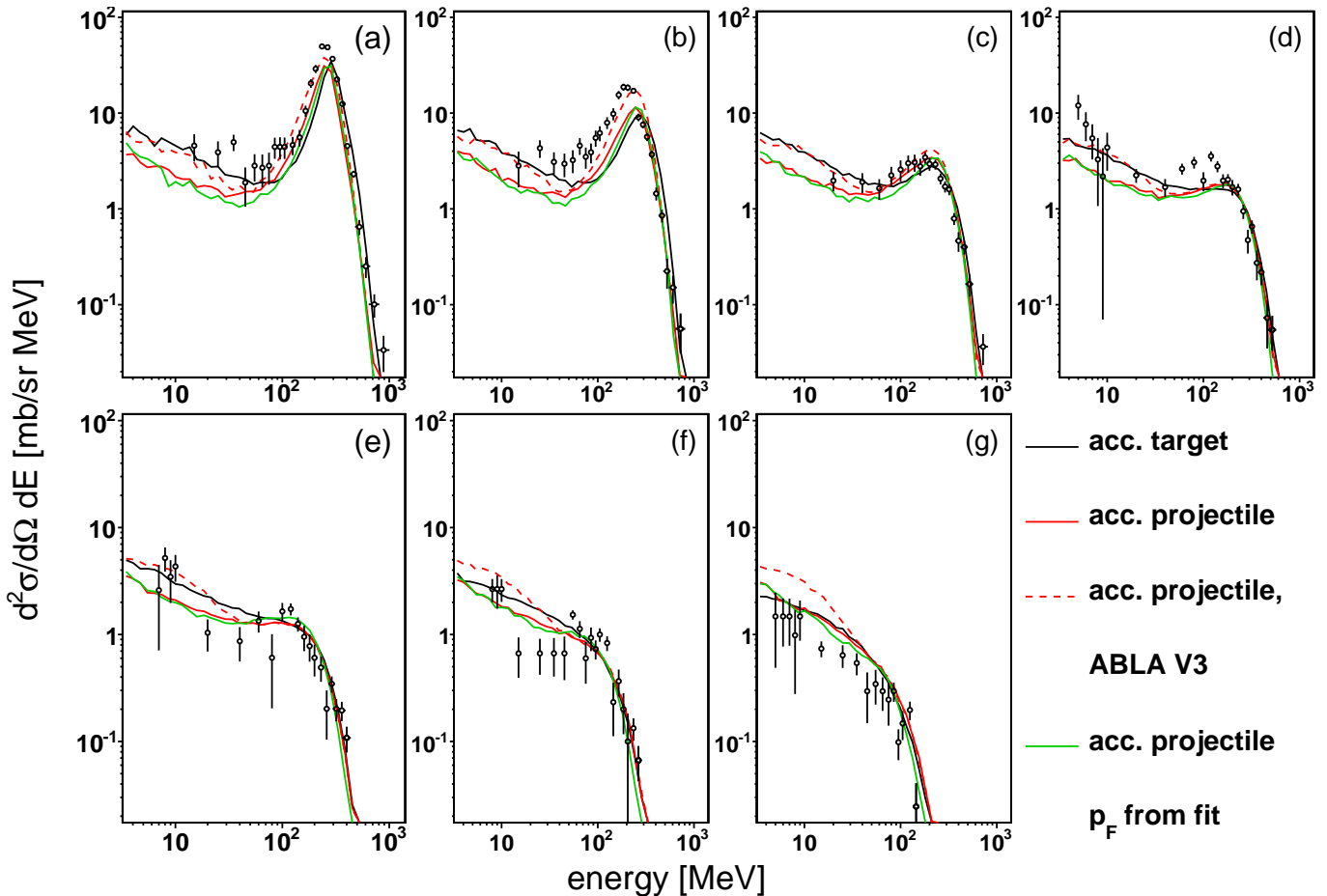


Figure 14. (Color online) Double-differential cross sections for neutron production at (a)  $5^\circ$ , (b)  $10^\circ$ , (c)  $20^\circ$ , (d)  $30^\circ$ , (e)  $40^\circ$ , (f)  $60^\circ$  and (g)  $80^\circ$ , from a 290-AMeV  $^{12}\text{C}+\text{C}$  reaction. The INCL++ calculations are presented in accurate-target (black lines) and accurate-projectile (solid red lines) mode, coupled with the G4ExcitationHandler de-excitation model. We also show an accurate-projectile calculation with ABLA V3 (dashed red lines) and a calculation with a modified value of the Fermi momentum (green lines, see text). Experimental data are taken from Ref. 75.

the  $^4\text{He}$ -induced reaction). All models use the same de-excitation (G4ExcitationHandler), except Bertini, which has its own internal de-excitation module.

One notices that the BIC predictions are generally in less good agreement with the experimental data than INCL++. The QMD results are everywhere comparable to or worse than the INCL++ calculation, except at the forward-most angles, which were shown to be improvable in INCL++ by using the empirical Fermi momentum. Note also that the CPU time for QMD is about two orders of magnitude larger than for INCL++. All the other models fail to describe the  $^4\text{He}$ -fragmentation peak, which (in view of the above) might suggest that they employ unrealistic Fermi momenta for this projectile. In addition, the BIC model shows some unphysical structures at small angles for the  $^4\text{He}+\text{Cu}$  system.

We now turn to the production of charged particles. We focus in particular on a recent experiment by Dudouet *et al.* [78, 83], who measured double-differential cross sections for the production of several charged par-

ticles from reactions induced by a 95-AMeV  $^{12}\text{C}$  beam on targets ranging from hydrogen to titanium. We are mostly interested in the carbon-target data for the purpose of verifying the INCL++ nucleus-nucleus extension and assessing the severity of the projectile-target asymmetry (see Section II D). Calculations with some Geant4 models have been presented in Ref. 84, where however the authors used INCL++ v5.1.9, which was shown above to be affected by serious drawbacks for the  $^{12}\text{C}+^{12}\text{C}$  reaction (Fig. 13). Our results can be reproduced using Geant4 v10.0 and should be considered as references.

First, we observe that the incident energy (95 AMeV) is rather low. The conditions for the applicability of the intranuclear-cascade hypothesis (independent binary nucleon-nucleon collisions) are not very well fulfilled here. Figure 13 indicates that the reaction cross section predicted by INCL++ is in excess of the experimental value by about 30% at this energy. Note also that INCL++'s low-energy fusion sector is responsible for 43% of the reaction cross section, which is far from negligible. Given

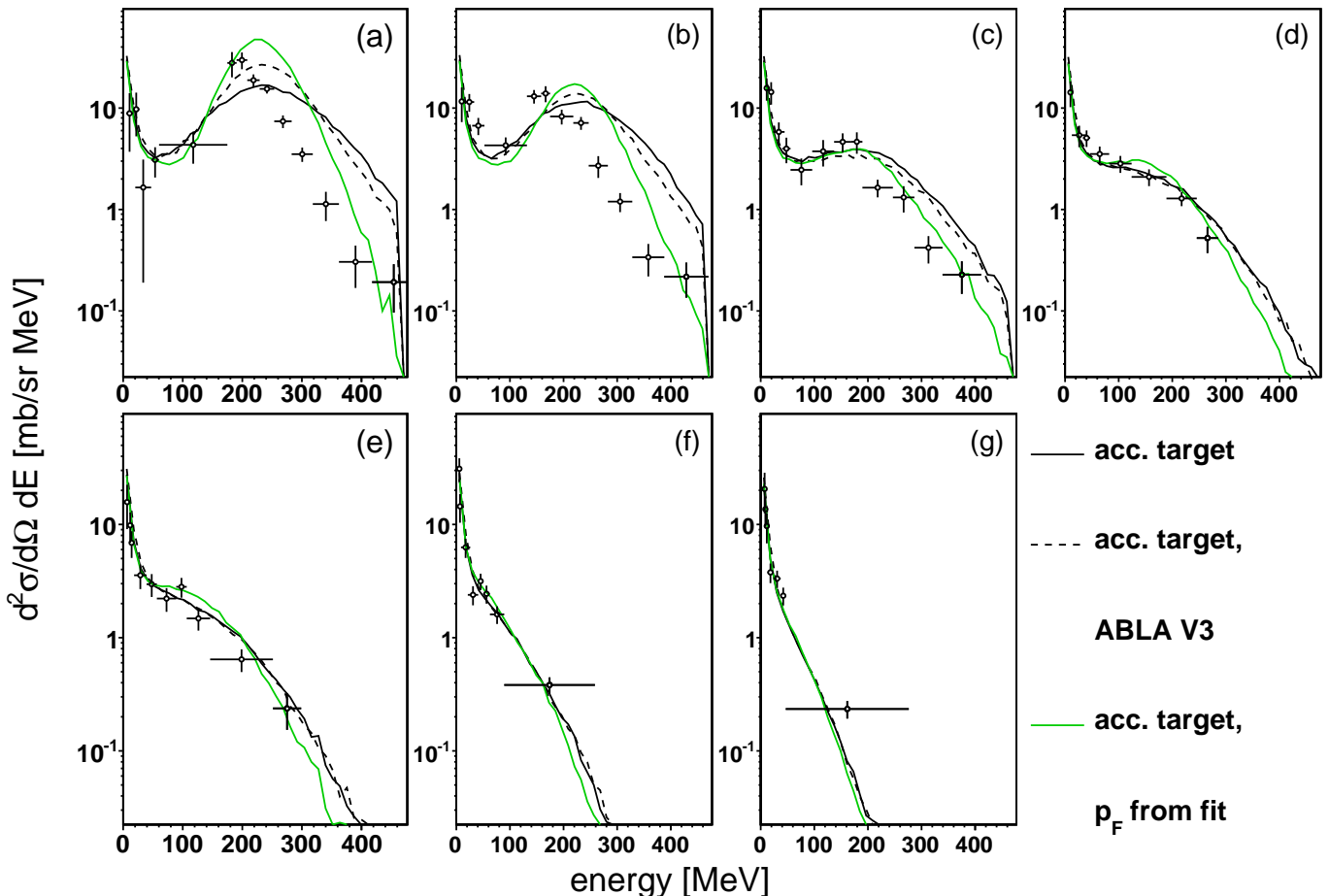


Figure 15. (Color online) Double-differential cross sections for neutron production at (a)  $4^\circ$ , (b)  $9^\circ$ , (c)  $20^\circ$ , (d)  $30^\circ$ , (e)  $40^\circ$ , (f)  $60^\circ$  and (g)  $80^\circ$ , from a 230-AMeV  $^4\text{He}+\text{Cu}$  reaction. The INCL++ calculations are presented in accurate-target mode (solid black lines), coupled with the G4ExcitationHandler de-excitation model. We also show a calculation with ABLA V3 (dashed black lines) and a calculation with a modified value of the Fermi momentum (green lines, see text). Experimental data are taken from Ref. 77.

the empirical nature of the fusion sector, we do not expect very accurate predictions.

Since the 95-AMeV  $^{12}\text{C}+\text{C}$  reaction is essentially symmetric, we shall use this example to illustrate random symmetrization, as described in Section IID.

Figure 18 shows angular-differential cross sections for the production of protons,  $^4\text{He}$ ,  $^7\text{Li}$  and  $^{11}\text{C}$ . For each angle, the calculated ejectile energy distributions were integrated above the detection thresholds reported by Dudouet *et al.* [Table IV in 83].

It is striking that none of the considered models can accurately reproduce all the experimental data (see however calculations with LAQGSM [65]). The proton angular distributions predicted by INCL++ (either in accurate-projectile or in accurate-target mode) are quite close to the experimental data; the accurate-projectile and accurate-target predictions are again very similar, which confirms the remark made about Fig. 14.

The agreement progressively degrades as the mass of the ejectile increases, especially for the calculation in accurate-target mode. Dudouet *et al.* [83] showed

that the experimental angular distributions can be represented as a sum of a Gaussian and an exponential contribution and claimed [84] that no model can reproduce this trend. Figure 18 shows that this is incorrect: although the exponential tail of the angular distribution might be quantitatively incorrect (especially for  $^{11}\text{C}$ ), INCL++ in accurate-projectile mode is clearly the only model that can capture the trend of the experimental data. In spite of the crudeness of the model ingredients, the agreement with the experimental data is remarkable, except for the case of  $^{11}\text{C}$ .

Since the accurate-projectile results are generally closer to the experimental data than the accurate-target calculations, there is not much to be gained here by applying random symmetrization. The results of randomly symmetrized calculations, which are shown in Fig. 18 and which are simply averages of the accurate-projectile and accurate-target results, are *a fortiori* in good agreement with the experimental data for protons, but they are less good than the results in accurate-projectile mode for all the other ejectiles.

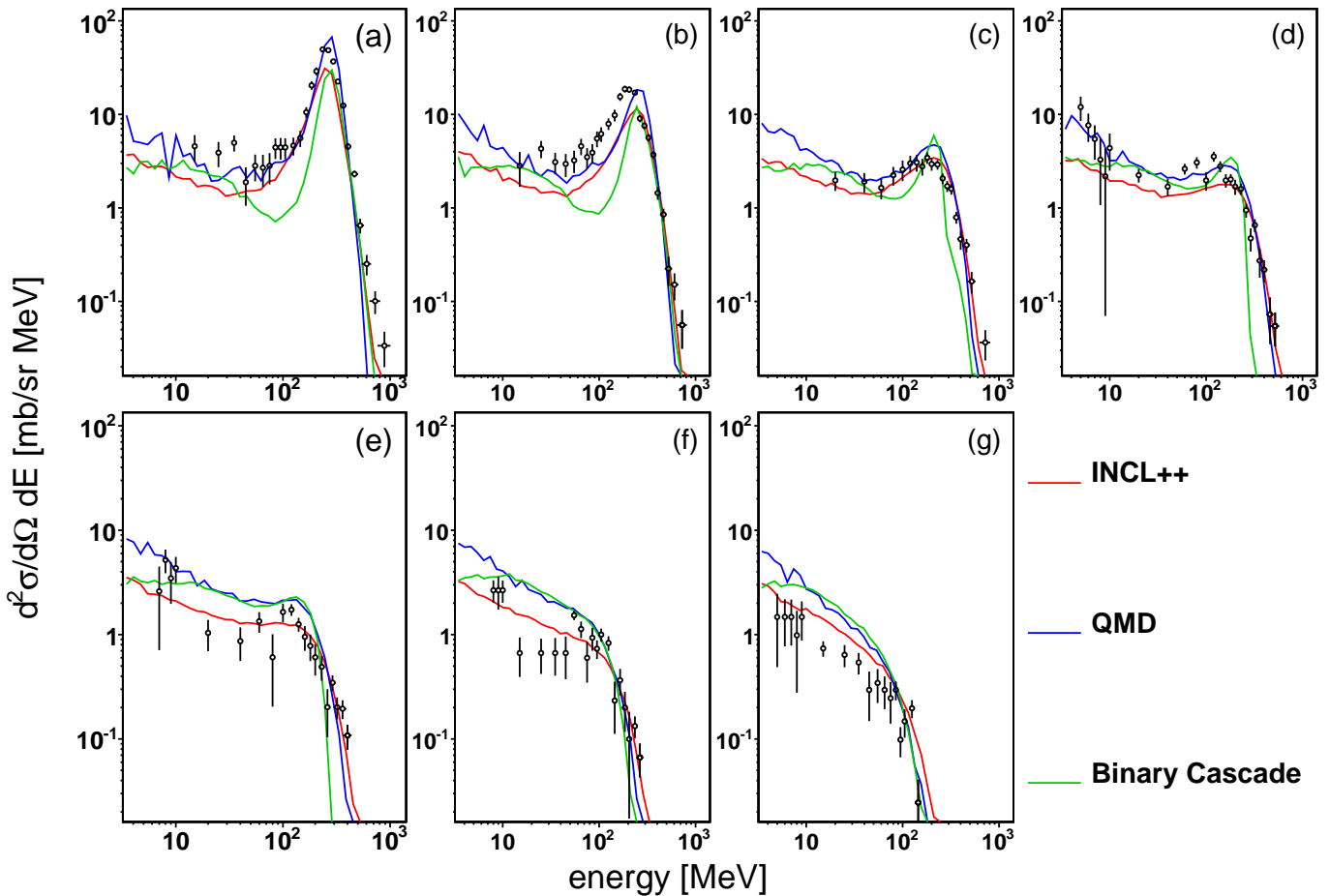


Figure 16. (Color online) Same as Fig. 14 for INCL++ (accurate-projectile mode, red lines), Geant4’s QMD model (blue lines) and BIC model (green lines). All models are coupled to G4ExcitationHandler.

As far as the other models are concerned, QMD seems to systematically underpredict the fragment yields at small angles. In general, the shape of the angular distribution is very different from the experimental result. Even for protons one can observe a sizable overestimation of the yield. The BIC results manage to capture at least some qualitative features of the experimental data, but its predictions are in general less accurate than those of INCL++.

Double-differential spectra for the same ejectiles are shown in Figs. 19–22. Here we notice larger discrepancies than in Fig. 18, even for the INCL++ calculation in accurate-projectile mode. For example, no model can reproduce the slope of the high-energy tail of the proton spectra at all angles. Experimental fragment spectra show a mid-rapidity component that is not reproduced by any of the models, although INCL++ is much closer to the data than the others. The randomly-symmetrized calculations are especially good on the spectra for  $^4\text{He}$  nuclei, Fig. 20. At large angles, the INCL++ spectra show a broad bump that is not seen in the data and that is the continuation of the projectile-like fragmentation peak at  $4^\circ$ . In other words, the projectile-like fragments seem to

pick up too much transverse momentum from the collision, which results in a too broad angular distribution. This obviously indicates that the model fails to properly describe some aspects of projectile fragmentation.

#### D. Rapidity spectra and projectile-target asymmetry

In addition to and independently of the comparison with the experimental data, we present in Figs. 23 and 24 the rapidity spectra of particles emitted in  $^{12}\text{C}+^{12}\text{C}$  respectively at 100 and 400 AMeV laboratory energy, which we can use to assess the severity of the projectile-target asymmetry in INCL++. The results of calculations performed with BIC and QMD are also shown. A perfectly projectile-target symmetric model produces distributions that are symmetric around the dotted mid-rapidity line, which is located at half of the nominal rapidity of the projectile.

Visual inspection of Figs. 23–24 reveals violations of the projectile-target symmetry in INCL++ and BIC. Still, it is clear that INCL++ is approximately symmet-

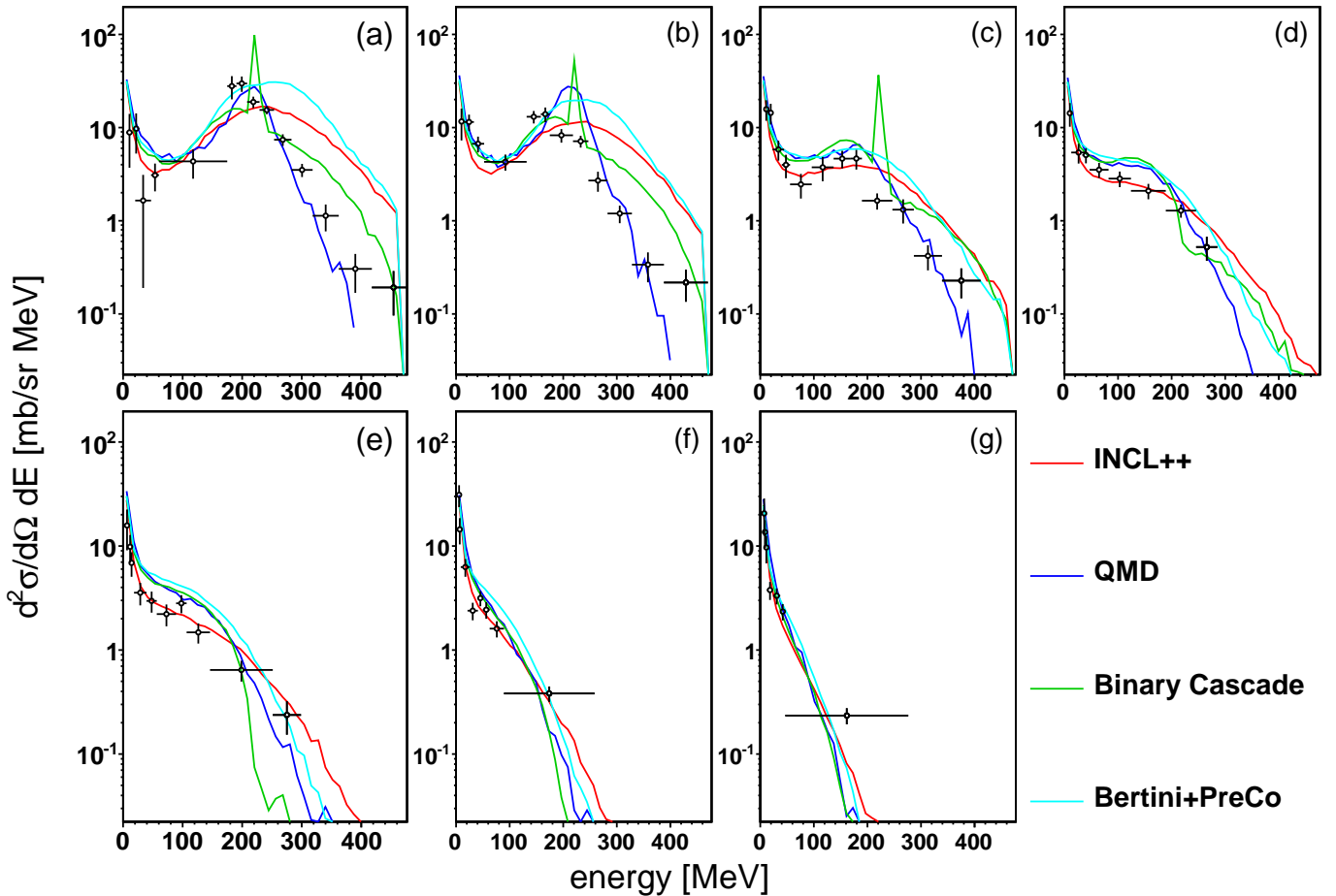


Figure 17. (Color online) Same as Fig. 15 for INCL++ (accurate-projectile mode, red lines), Geant4’s QMD model (blue lines), BIC (green lines) and Bertini+PreCompound (cyan lines) models. All models except Bertini+PreCompound are coupled to G4ExcitationHandler.

ric for protons (as discussed above) and progressively degrades as the ejectile mass increases. The results of QMD are fully symmetric, which is a consequence of the fact that the model treats all nucleons on the same footing.

### E. Fragmentation cross sections

We finally turn to the analysis of fragmentation cross section. In keep with our approach to the validation of nucleon-induced reactions, we focus on measurements of isotopic cross sections in inverse kinematics. The advantage of such data sets is that they provide a comprehensive picture of the reaction mechanism. The accurate fragmentation data on hydrogen targets taken using the Fragment Separator at GSI (Darmstadt, Germany) [e.g. 43, 85, 86] have often proved invaluable for the study of the nucleon-nucleus reaction mechanism and for the optimization of de-excitation models.

Unfortunately, the coverage for reactions on light nuclei is not as extensive as for hydrogen. Beryllium is often exploited as a production target in the search for

exotic neutron-rich [e.g. 7] or neutron-poor [e.g. 8] nuclei, but there exist only few experiments where essentially all projectile-like fragments were covered. We chose to limit our comparison to such extensive experimental datasets.

The data for 1 AGeV  $^{208}\text{Pb}$  on deuterium [87], although only marginally relevant for the assessment of INCL++’s nucleus-nucleus extension, are perhaps the most complete. Figure 25 shows the mass distributions of the fragments. Note that the model predictions are obtained by summing up the isotopic cross sections only over the isotopes that were detected in the experiment; this is the reason of the dip around  $A = 115$ .

One immediately observes that the model predictions are very sensitive to the choice of the de-excitation model. The distribution of spallation residues ( $A > 115$ ) is accurately described only by INCL++/ABLA07 and INCL++/ABLA V3 (except very close to the projectile mass 208). Models coupled with G4ExcitationHandler systematically underestimate the yields for deep spallation residues ( $115 < A \lesssim 160$ ). All the models overestimate the cross sections for the fission products ( $A < 115$ ) by a factor of 2-4. This was already the



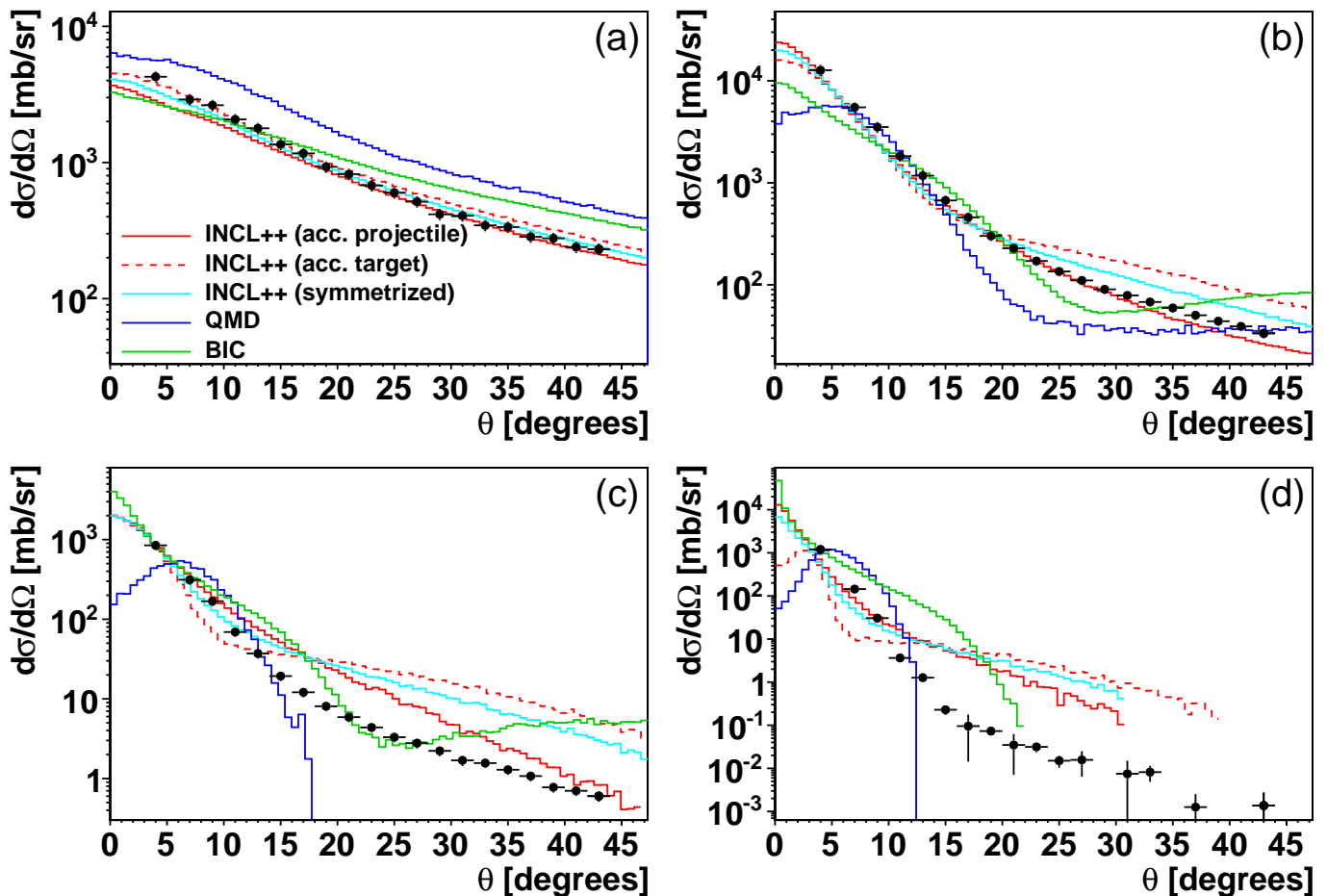


Figure 18. (Color online) Angle-differential cross section for the production of (a) protons, (b)  ${}^4\text{He}$ , (c)  ${}^7\text{Li}$  and (d)  ${}^{11}\text{C}$  from the 95-AMeV  ${}^{12}\text{C}+{}^{12}\text{C}$  reaction. Calculations with INCL++ (accurate-projectile mode, solid red lines; accurate-target mode, dashed red lines; randomly symmetrized, cyan lines), QMD (blue lines) and BIC (green lines) are shown. Experimental data are taken from Ref. 78.

case with INCL4.2 [Fig. 23 in 23]. The overestimation of INCL++/ABLA07's and INCL++/ABLA V3's predictions should probably be related to the underestimation around  $A = 195$ ; it has been shown [88] that fissioning nuclei belong exactly to this mass range.

Figure 26 shows a few isotopic distributions from the fission region. The distributions predicted by G4ExcitationHandler and Bertini's fission module systematically overpredict the peak height; if one rescaled the distributions to match the experimental peak height, the tails would be underestimated, i.e. the distributions are too narrow. Moreover, the peak position is slightly shifted to the neutron-rich side. On the other hand, the INCL++/ABLA07 and INCL++/ABLA V3 predictions have more or less the correct shape. This suggests that it should be possible to reproduce the data in Fig. 25 by acting on the competition between fission and evaporation in ABLA07 or ABLA V3. Compared to the  ${}^{208}\text{Pb}+{}^1\text{H}$  data in Fig. 5, the  ${}^{208}\text{Pb}+{}^2\text{H}$  reaction explores higher excitation energies and should be more sensitive to dissipative effects in the fission dynamics [89], for instance.

Figure 27 shows some isotopic distributions in the region of the spallation residues. Again, the predictions by INCL++/ABLA07 and INCL++/ABLA V3 are rather close to the experimental data, while the other models systematically overestimate the  $N/Z$  ratio of the residues.

As far as reactions on light nuclei are concerned, isotopic fragmentation cross sections have been measured by Weber *et al.* [90] for 500 AMeV  ${}^{86}\text{Kr}+{}^9\text{Be}$ . The mass distribution and some isotopic distributions are shown in Figs. 28 and 29. Again, note that only the *measured* isotopes contribute to the model predictions for the mass distribution.

The mass distribution of fragments is again mostly sensitive to the choice of the de-excitation model. The INCL++/ABLA07 can reproduce most of the experimental data fairly well, but it underestimates the production of fragments close to the projectile  ${}^{86}\text{Kr}$ . QMD performs slightly better close to the projectile but slightly worse at intermediate mass ( $A \simeq 35$ ). The INCL++/G4ExcitationHandler and

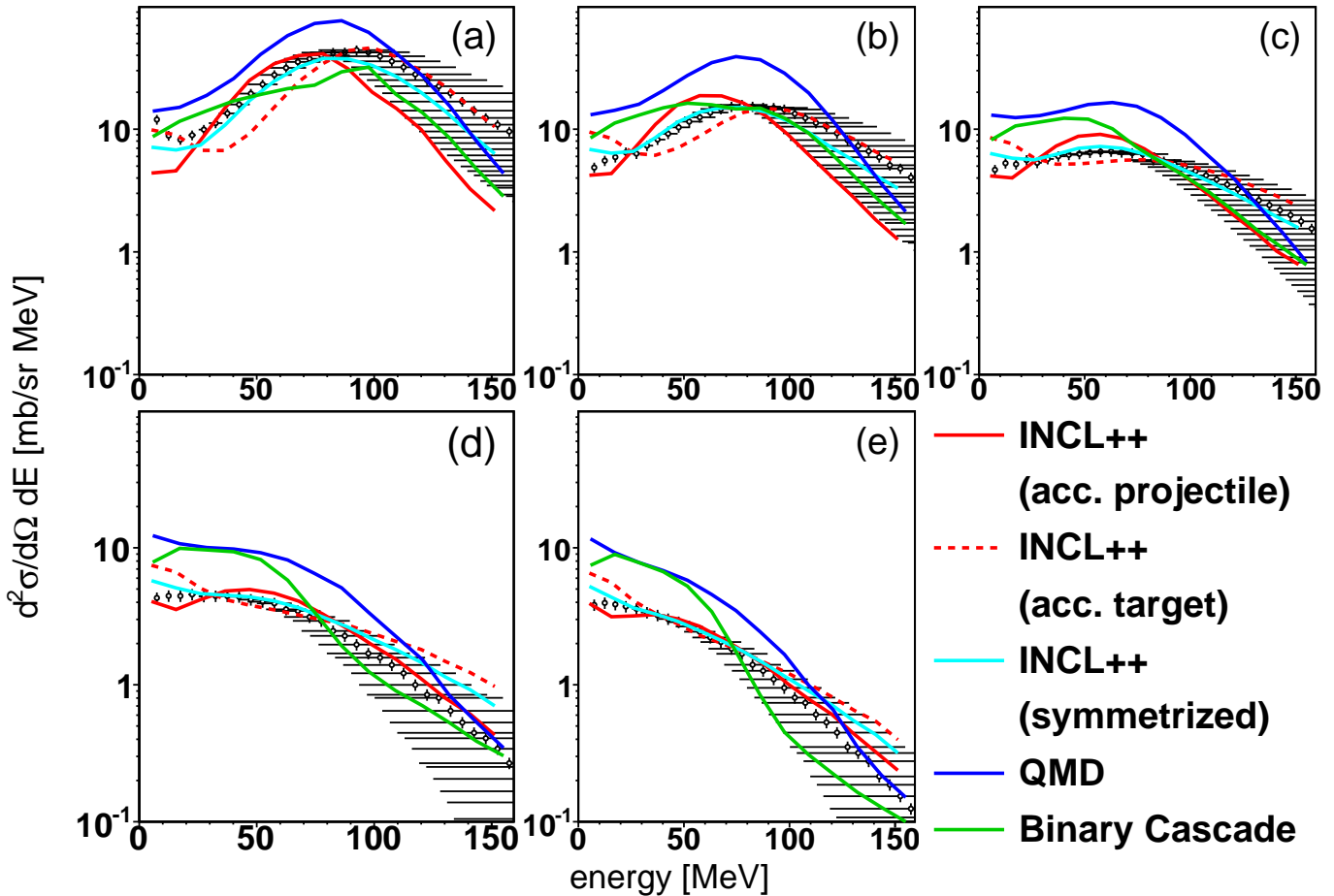


Figure 19. (Color online) Double-differential cross sections for the production of protons at (a)  $4^\circ$ , (b)  $13^\circ$ , (c)  $21^\circ$ , (d)  $29^\circ$  and (e)  $43^\circ$ , from the 95-AMeV  $^{12}\text{C}+^{12}\text{C}$  reaction. Calculations with INCL++ (accurate-projectile mode, solid red lines; accurate-target mode, dashed red lines), QMD (blue lines) and BIC (green lines) are shown. Experimental data are taken from Ref. 78.

BIC/G4ExcitationHandler couplings well reproduce the data for  $A > 40$ , but overestimate the cross sections for lighter fragments. The INCL++/ABLA V3 coupling, finally, largely overestimates the cross section for the lightest fragments.

The large difference between ABLA V3 and ABLA07 can be explained by the fact that evaporation channels in ABLA V3 are limited to proton, neutron and alpha. ABLA07, on the other hand, can simulate the emission of any fragment up to half of the mass of the excited nucleus. Also, G4ExcitationHandler can evaporate fragments up to  $^{28}\text{Mg}$  and can be considered to be intermediate between ABLA V3 and ABLA07. Thus, the predicted cross sections in the  $A < 40$  region seem to correlate well with the models' maximum ejectile mass. The QMD/G4ExcitationHandler coupling respects this trend to a degree for fragment masses above  $\sim 25$ .

The isotopic distributions in Fig. 29 illustrate that INCL++/ABLA07 is affected by a defect. The yields for neutron-rich isotopes of  $Z > 25$  nuclei are systematically overestimated. This defect might be correlated with

the underestimation of the cross sections for the heaviest fragments. Given that ABLA07 is probably the most sophisticated of the de-excitation models considered, one might be tempted to conclude that defects in the predicted isotopic yields are actually due to intranuclear cascade; however, INCL++/G4ExcitationHandler does not exhibit the same defect, but QMD/G4ExcitationHandler does. The emerging picture is unclear and no conclusion can be drawn. We have anyway verified that the overestimation of the neutron-rich isotopes is not due to the neglect of Pauli blocking on the first collision in the projectile. This is reasonable in the light of the QMD/G4ExcitationHandler results, which are surprisingly similar to those of INCL++/ABLA07 on the neutron-rich sides of the isotopic distributions, but must be generated by a completely different dynamics.

Similar conclusions can be drawn from the results at lower beam energy. We show in Figs. 30 and 31 the comparison between the model predictions and the experimental data for 140-AMeV  $^{58}\text{Ni}+^9\text{Be}$  [91, 92]. Note that at this energy only about 10% of the reaction cross

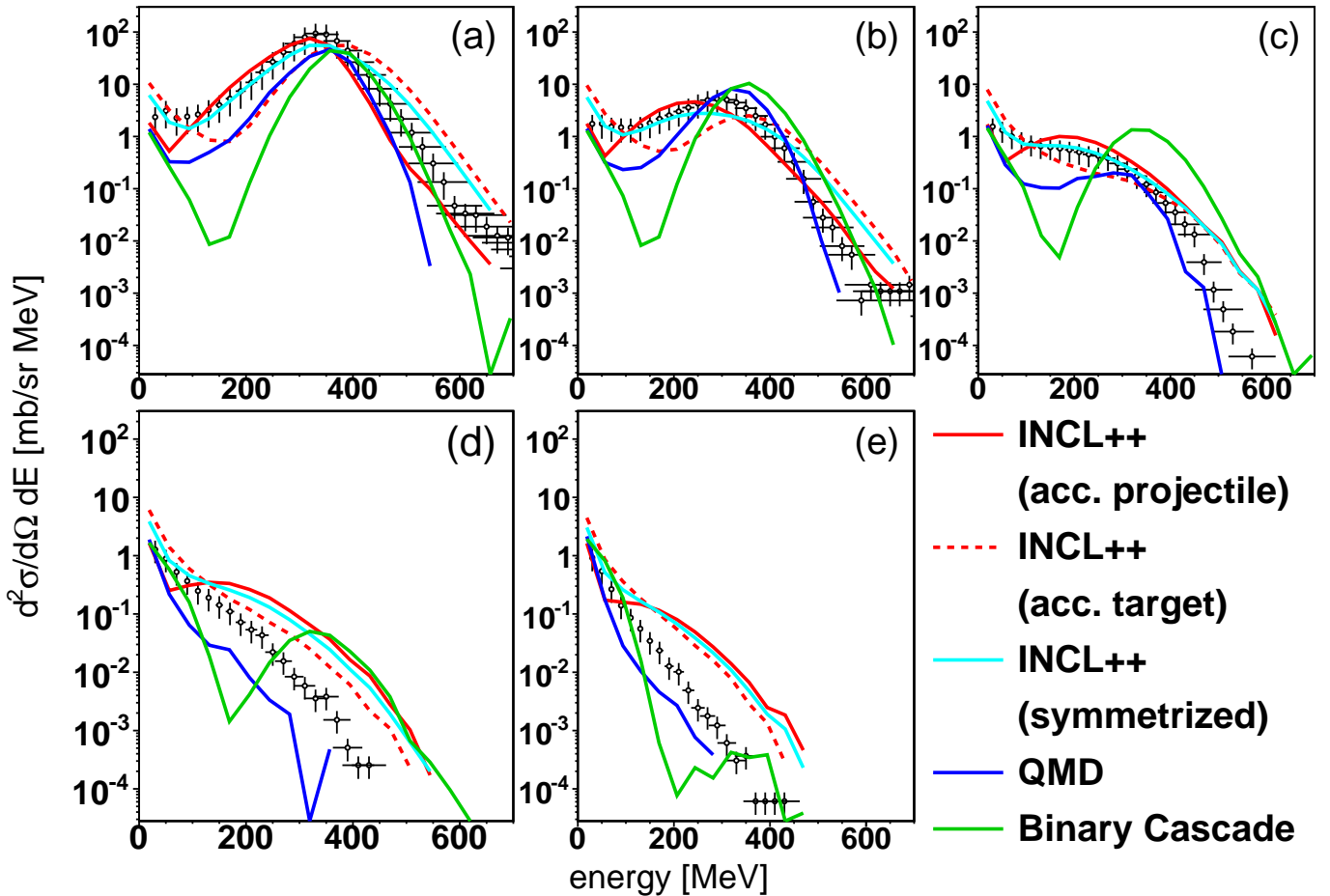


Figure 20. (Color online) Same as Fig. 19, for  ${}^4\text{He}$  ejectiles.

section is generated by INCL++'s low-energy fusion sector.

Again, most of the mass distribution is best predicted by INCL++/ABLA07, with the exception of nuclei close to the projectile  ${}^{58}\text{Ni}$ . The INCL++/G4ExcitationHandler result is similar but slightly less good (the  $A = 17$  cross section is largely overestimated, but all the yield comes from the single isotope  ${}^{17}\text{O}$ ). The BIC/G4ExcitationHandler and QMD/G4ExcitationHandler couplings are yet less good, and INCL++/ABLA V3 is overall the worst. This is easy to understand if one remembers that ABLA V3 cannot evaporate intermediate-mass fragments, which occur most abundantly in light systems (such as  ${}^{58}\text{Ni}$  and  ${}^{86}\text{Kr}$ ).

The INCL++-based calculations systematically overestimate the cross sections for very small mass losses ( $\Delta A = 1$  or  $2$ ). It would be tempting to interpret this in terms of lacking Pauli blocking on the first collision in the Fermi sea of the cascade projectile. We have indeed verified that these cross sections are decreased by roughly 10–20% if Pauli blocking in the projectile is introduced (not shown in Figs. 30 and 31). This is however insufficient to cure the overestimation, which in the worst case

Table III. Average characteristics of the projectile-like cascade remnant for the reactions studied in Section IV E.

reaction	$A$	$Z$	excitation energy per nucleon (MeV)	spin ( $\hbar$ )
140-AMeV ${}^{58}\text{Ni}+{}^9\text{Be}$	56.6	27.2	2.3	33.6
500-AMeV ${}^{86}\text{Kr}+{}^9\text{Be}$	76.6	32.0	3.0	37.1
1000-AMeV ${}^{208}\text{Pb}+{}^2\text{H}$	199.6	78.7	1.2	22.9
1050-AMeV ${}^{56}\text{Fe}+{}^{12}\text{C}$	44.9	20.8	6.8	60.0

(the yield for  $A = 57$ ) is close to a factor of 2.5.

The isotopic distributions in Fig. 31 are qualitatively similar to those of Fig. 29, but one has to bear in mind that the experimental coverage is less extensive here. It is difficult to verify if INCL++/ABLA07 and QMD/G4ExcitationHandler overestimate the yields for neutron-rich residues, as they do in 500-AMeV  ${}^{86}\text{Kr}+{}^9\text{Be}$ .

We conclude this section by discussing the model predictions for partial charge-changing cross sections for a 1.05  $A$ -GeV  ${}^{56}\text{Fe}$  projectile colliding with a  ${}^{12}\text{C}$  target [93]. Of all the reactions so far considered,  ${}^{56}\text{Fe}+{}^{12}\text{C}$

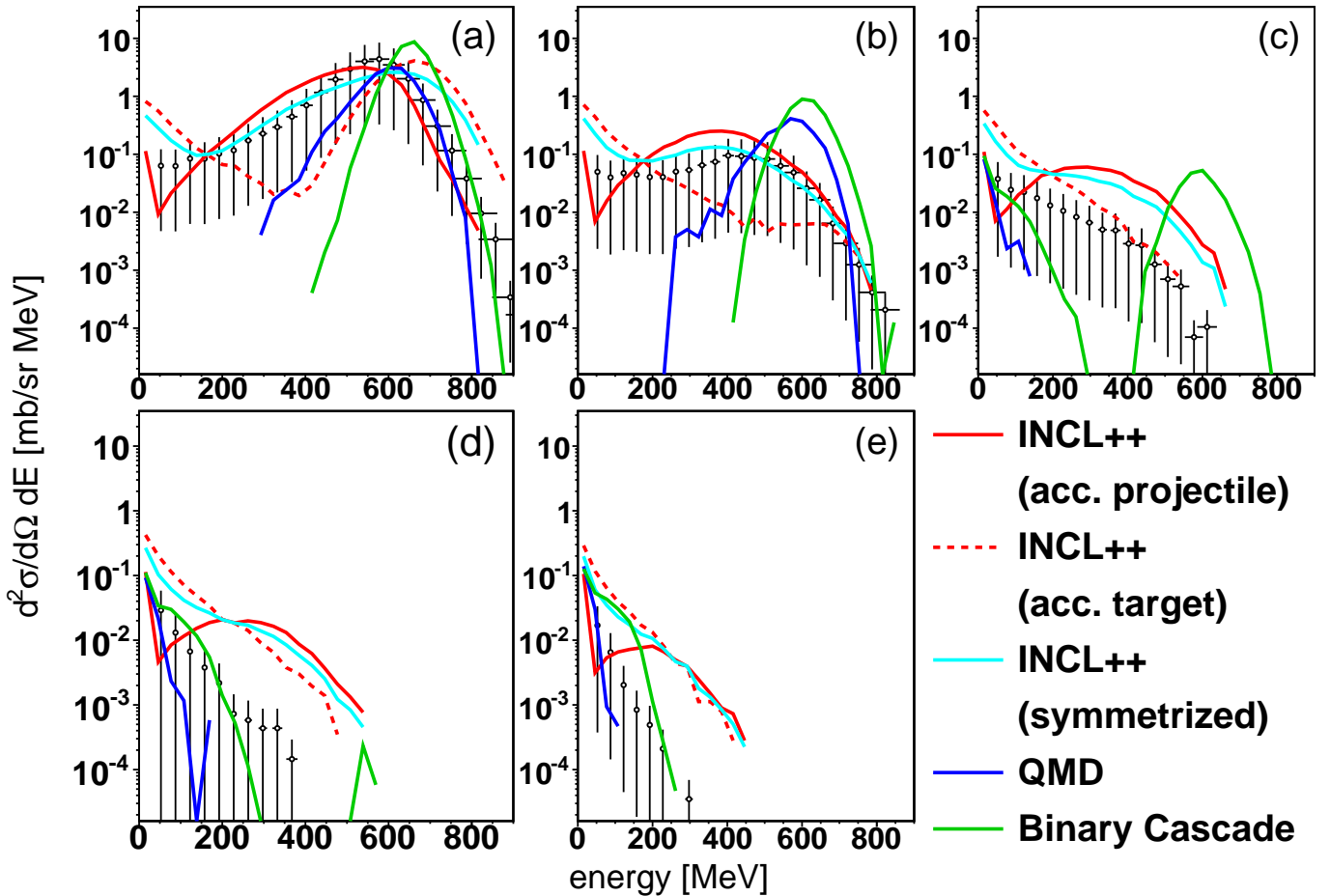


Figure 21. (Color online) Same as Fig. 19, for  ${}^7\text{Li}$  ejectiles.

is the one that leads to the highest excitation energies per nucleon, due to the high kinetic energy and the relatively small size of the projectile nucleus. This is illustrated by Fig. 33, which compares the distributions of the excitation energy of the projectile-like cascade remnants, as calculated by INCL++, for all the reactions studied in this section. The average excitation energies are reported in Table III. At sufficiently large excitation energy, multifragmentation is expected to become the dominant de-excitation mechanism. Among the considered de-excitation models, ABLA07 is the only one to feature a semi-empirical treatment of multifragmentation. The G4ExcitationHandler model does include a multifragmentation module, but it is deactivated by default.

The model calculations are compared with the experimental data in Fig. 32. One remarks that the INCL++/ABLA V3 prediction is poor. We have already observed above that ABLA V3 is not suitable for systems for which there is a large probability of evaporating intermediate-mass fragments. The 1.05 AGeV  ${}^{56}\text{Fe}+{}^{12}\text{C}$  reaction surely falls within this category. The INCL++/G4ExcitationHandler and BIC/G4ExcitationHandler predictions are quite simi-

lar and in good agreement with the data, while the QMD/G4ExcitationHandler cross sections are slightly too large. Finally, INCL++/ABLA07 is close to the experimental data for  $Z \gtrsim 19$ , but severely underpredicts the data for the smallest charges.

It is perhaps surprising to observe that the cross sections for large charge losses are best reproduced using de-excitation models that *neglect* multifragmentation. ABLA07 is the only model that somehow tries to handle this mechanism, but the comparison with the data seems to indicate that its semi-empirical treatment is inadequate for the very large excitation energies that can be reached in this reaction. On the other hand, it is known that sequential binary decay can generate fragment partitions that are similar to those generated by multifragmentation [94]. More discriminating observables would be needed to illustrate the difference between the two de-excitation modes.

## F. Summary

For the benefit of the reader, we shall now try to condense the vast amount of information about nucleus-



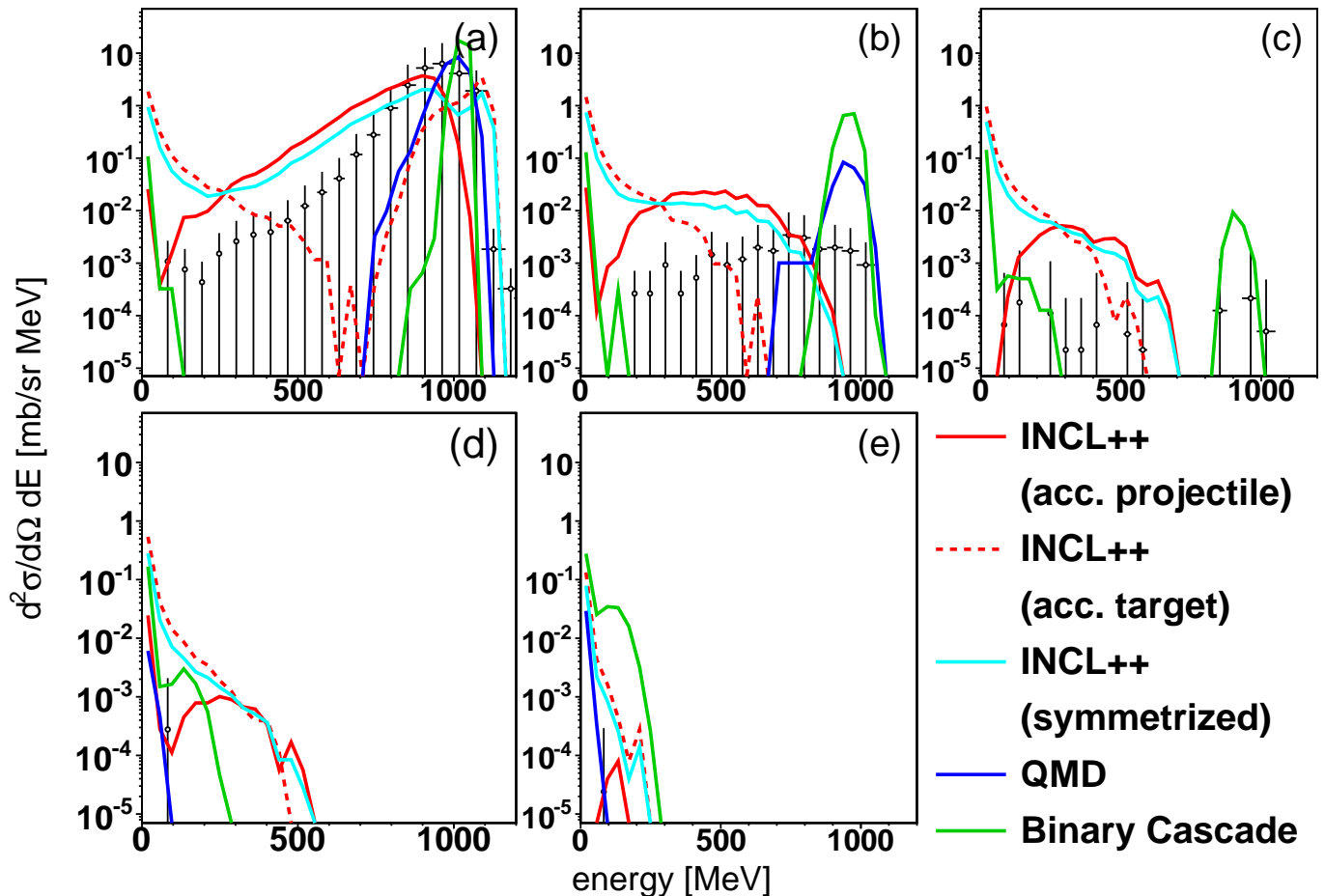


Figure 22. (Color online) Same as Fig. 19, for  $^{11}\text{C}$  ejectiles.

nucleus reactions that we have presented in this section into a few general observations. Our summary might contain some degree of subjectivity, but it should be read as an attempt to guide users of reaction models towards the best choice for their needs. Our conclusions are also based on the results of other comparisons with experimental data that have been omitted for the sake of conciseness.

As far as neutron production is concerned, the choice of the de-excitation model generally represents a second-order effect, except for the case of very light projectiles (say alphas and lighter). The most accurate reproduction of the experimental data is probably guaranteed by QMD. Still, INCL++ is very close to QMD in terms of quality (and sometimes better in specific kinematical regions; Figs. 16–17), while being much faster. For very light projectiles, the choice of the Fermi momentum can play an important role in the projectile-fragmentation kinematical region (Fig. 15).

The scenario for proton production is less detailed than the neutron case because of the limited experimental coverage. Nevertheless, for reasons that are not clear to us, QMD seems to perform less well than for neutrons, which is rather surprising. The INCL++ predictions are

of rather good quality (Figs. 18–19).

Light charged particles are best reproduced by INCL++ (Figs. 18 and 20). This is somewhat expected, since INCL++ is the only dynamical model considered to include a dedicated mechanism for LCP production. QMD’s nucleon-nucleon interaction is able to coalesce escaping nucleons, but it is known that the resulting LCP spectra are not in good agreement with the experimental data [96]. Note that the choice of the de-excitation model is very important for this observable, insofar as ABLA V3 can only evaporate neutrons, protons and alphas.

The production of residual nuclei is in general sensitive to the choice of the de-excitation model, except for small mass losses with respect to the pre-fragment. Generally speaking, ABLA V3 and ABLA07 have a long historical record of applications to the de-excitation of heavy nuclei (say  $A \gtrsim 150$ ) [e.g. 23]; as a consequence, the treatment of fission is quite sophisticated in both versions of the model. It should be stressed, however, that fission models typically contain a great deal of free parameters, which are sometimes adjusted in relation to a specific dynamical model. Because of this, the quality of the predictions of the very same fission model can vary wildly if different dynamical models are used in the entrance chan-

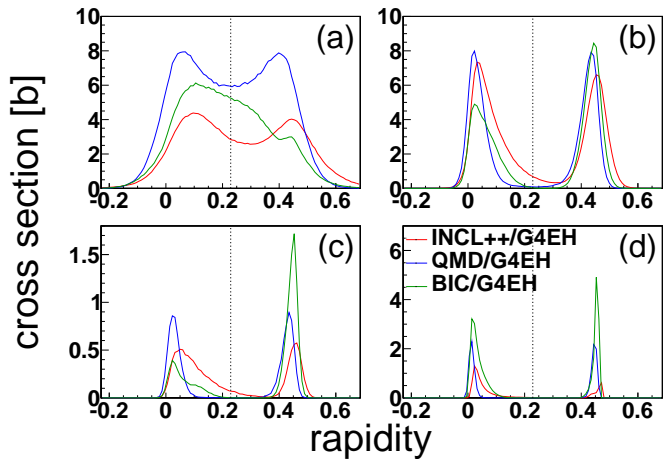


Figure 23. (Color online) Rapidity spectra of (a) protons, (b)  ${}^4\text{He}$ , (c)  ${}^7\text{Li}$  and (d)  ${}^{11}\text{C}$  fragments produced in 100-AMeV  ${}^{12}\text{C}+{}^{12}\text{C}$ , as calculated by INCL++/G4ExcitationHandler in accurate-target mode. The vertical dotted lines denote the central rapidity.

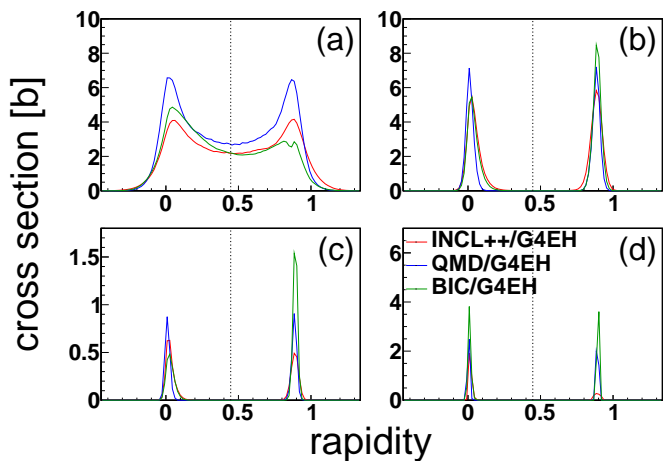


Figure 24. (Color online) Same as Fig. 23, for 400-AMeV  ${}^{12}\text{C}+{}^{12}\text{C}$ .

nel. Models of the ABLA family have often been used in conjunction with the INCL cascades and generally perform rather well in reactions induced by LCPs (Fig. 25) and especially in nucleon-nucleus reactions (Fig. 5). The fission parameters of the G4ExcitationHandler model have been adjusted in conjunction with BIC [37]; thus, the fission cross sections in Fig. 5 are correctly reproduced by BIC/G4ExcitationHandler (not shown in the figure, see Ref. 37), but they are overestimated by INCL++/G4ExcitationHandler. We are considering the possibility to restore the previous parameter values when coupling G4ExcitationHandler with INCL++; this should already yield better results in view of the fact that G4ExcitationHandler is rather similar to Furihata's GEM model [97] and the latter performs reasonably well with INCL4.6. Another option would be to perform an INCL-specific adjustment of the fission parameters.

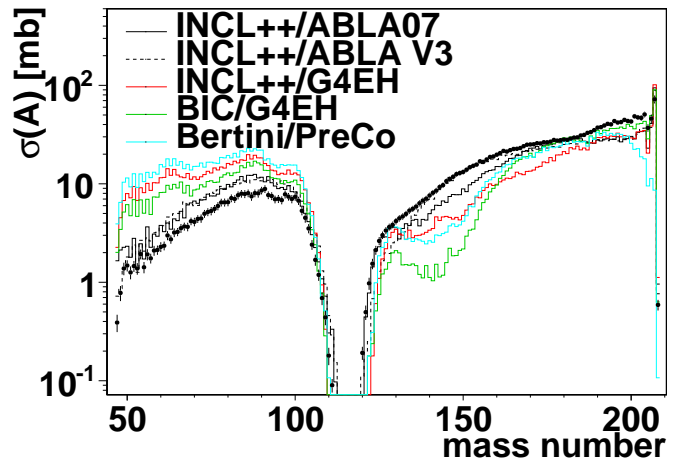


Figure 25. (Color online) Fragmentation cross sections for the 1-AGeV  ${}^{208}\text{Pb}+{}^2\text{H}$  reaction, as a function of the fragment mass number. Model calculations are compared to the data taken from Refs. 87 and 44. In the plot legend, *G4EH* stands for G4ExcitationHandler.

Finally, for nucleus-nucleus reactions, the possibility of large mass losses during the dynamical reaction stage makes the validation of fission models considerably more difficult; for these cases, the ABLA V3/ABLA07 fission models should globally offer acceptable performances.

The fragmentation of light nuclei ( $A \lesssim 150$ ) and the production of deep spallation residues from heavy nuclei generally require de-excitation mechanisms other than the conventional neutron-, proton- and alpha-evaporation channels. This is especially true in high-energy nucleon-nucleus reactions and even more so in nucleus-nucleus reactions, where the large pre-fragment excitation energies can favor the emission of small nuclei and/or induce multifragmentation. The ABLA V3 model is severely limited in this respect, insofar as it does not include evaporation of any particle with  $A > 4$ . Indeed, our comparison shows that INCL++/ABLA V3 is unsuitable for the description of the fragmentation of light systems (Figs. 28–32), even for small mass losses.

The other de-excitation models considered here (ABLA07 and G4ExcitationHandler) do not suffer from this limitation. The best agreement is generally observed for INCL++/ABLA07, except for systems where multifragmentation plays a major role. The BIC/G4ExcitationHandler, INCL++/G4ExcitationHandler and QMD/G4ExcitationHandler couplings produce predictions of similar fair quality and are all reasonable choices within the Geant4 framework. The CPU time is roughly of the same order of magnitude for BIC and INCL++, but it is typically much larger for QMD.

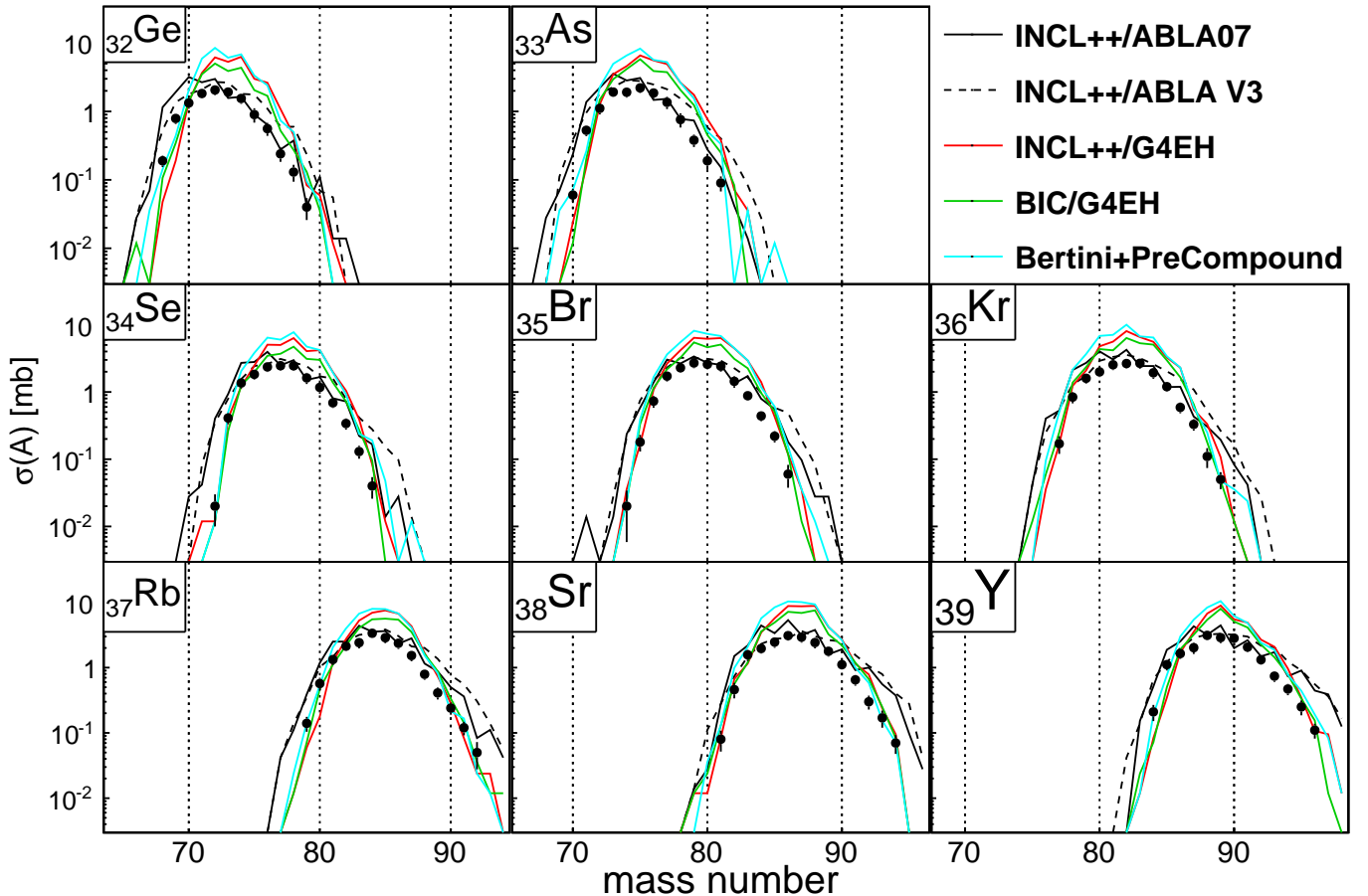


Figure 26. (Color online) Isotopic distributions from the fission region ( $32 \leq Z \leq 39$ ) for the 1-AGeV  $^{208}\text{Pb}+^2\text{H}$  reaction. Model calculations are compared to the data taken from Ref. 87. In the plot legend, *G4EH* stands for G4ExcitationHandler.

## V. CONCLUSIONS

We have presented for the first time the new C++ incarnation of the Liège Intranuclear Cascade model, a solid, modern code that is intended to be used as the base for any future development. The INCL++ code is feature-wise and physics-wise equivalent to its Fortran counterpart as far as nucleon- and pion-induced reactions are concerned. Small differences exist for reactions induced by light charged particles. The new code can be used for thick-target calculations through the Geant4 toolkit for particle transport.

The new INCL++ code can also accommodate reactions induced by light ions (up to  $A = 18$ ). We have described the crucial elements of the extension and we have discussed the limitations of our approach, which is admittedly more phenomenological than the core of the model. A broad comparison with heterogeneous observables has shown that, in spite of the conceptual difficulties, the extended INCL++ model yields predictions in fair agreement with the considered experimental data. In comparison to other models for nucleus-nucleus reactions available in Geant4, INCL++ stands out as one of the most viable options; it is however crucial (and we have

issued recommendations in this sense) to make a suitable choice for the coupling with the statistical de-excitation model. We conclude that our extended model is successful at capturing the physics that is essential for the description of inclusive observables from reactions induced by light nuclei.

Future work on INCL++ will proceed along several directions. First, we shall try to improve on the limits of the present nucleus-nucleus collision model, starting with the inclusion of Pauli blocking in the Fermi sea of the projectile. Second, we will work on providing an all-round well-performing model for Geant4 users, which should ideally combine the advantages of G4ExcitationHandler and ABLA07. Third, we will perform an extensive verification of the newly extended model in the 3–15 AGeV incident-energy range. Fourth, we plan to introduce the strangeness degree of freedom. This will provide the means to develop predictions for the production of kaons and hyperons and to simulate kaon-induced reactions. We ultimately aim at making predictions for the production of hypernuclei, although this also requires a strangeness-aware de-excitation model.

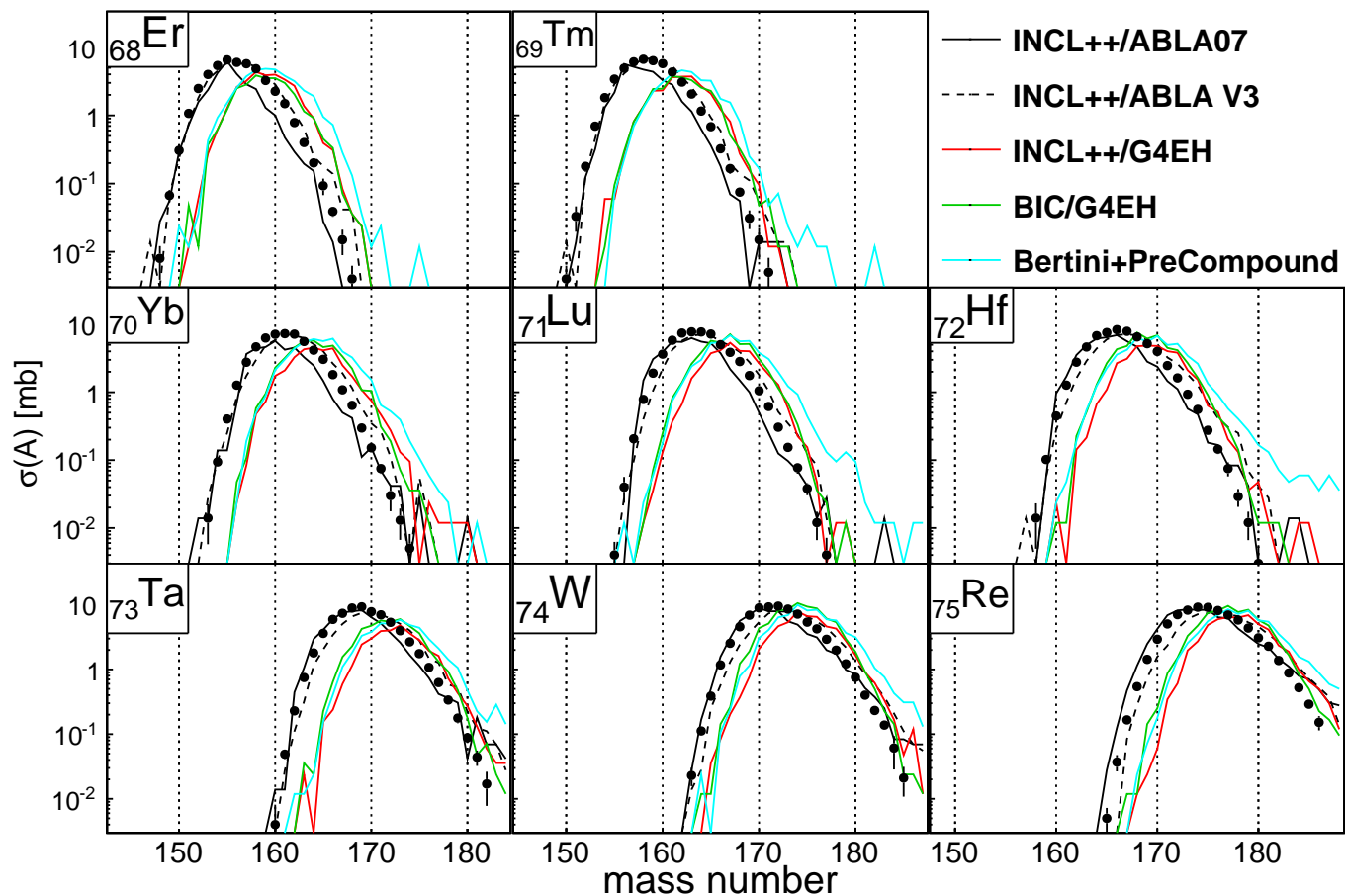


Figure 27. (Color online) Same as Fig. 26, for isotopic distributions from the spallation region ( $68 \leq Z \leq 75$ ).

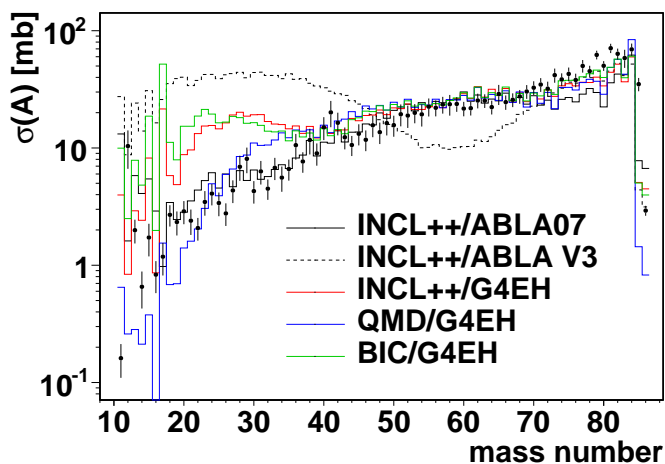


Figure 28. (Color online) Fragmentation cross sections for the 500-AMeV  $^{86}\text{Kr}+^9\text{Be}$  reaction, as a function of the fragment mass number. Model calculations are compared to the data taken from Refs. 90. In the plot legend,  $G4EH$  stands for  $G4ExcitationHandler$ .

## ACKNOWLEDGMENTS

This work has been partially supported by the EU ENSAR FP7 project (grant agreement 262010). We thank Dr. Stepan Mashnik for kindly directing us to the manuscript of Ref. 92.

## Appendix: INCL++ in Geant4

A stand-alone version of the INCL++ code is available on request via the official INCL web site. This code can simulate any thin-target reaction and produces output in ROOT format. Couplings to de-excitation models are also provided.

However, if one needs to simulate reactions in a thick absorber, the stand-alone code is not sufficient and one needs to turn to full-fledged particle-transport simulations. The Geant4 toolkit for particle transport has been including some version of the Liège Intranuclear-Cascade model since v9.1 (released in December 2007). The INCL++ code was first introduced in v9.5 (December 2011).

In recent versions of Geant4, it is possible to use the INCL++ model by selecting one of the following dedi-



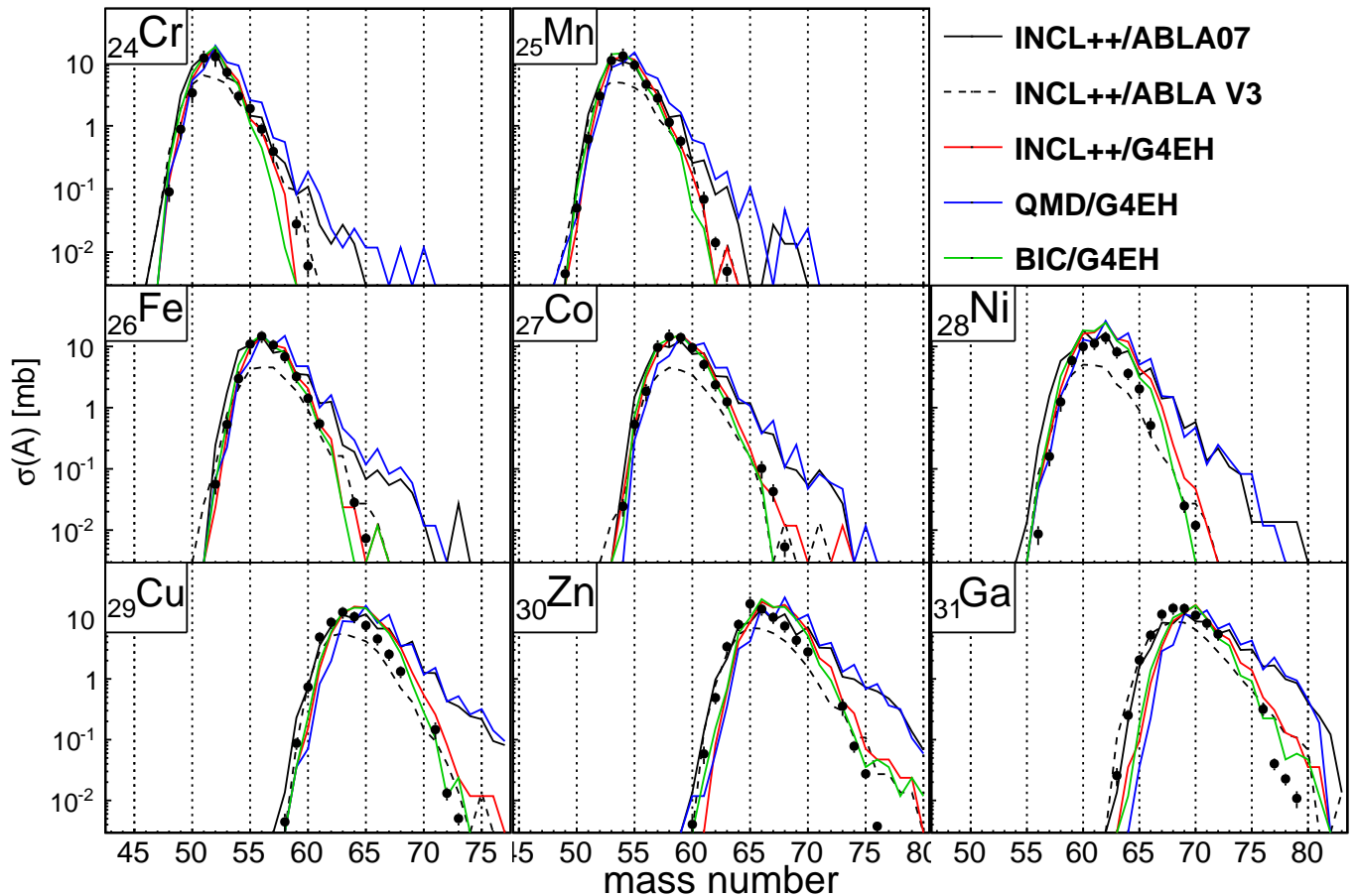


Figure 29. (Color online) Isotopic distributions ( $24 \leq Z \leq 31$ ) for the 500-AMeV  $^{86}\text{Kr}+^9\text{Be}$  reaction. Model calculations are compared to the data taken from Ref. 90. In the plot legend, *G4EH* stands for G4ExcitationHandler.

cated physics lists:

- QGSP\_INCLXX (available since v9.5)
- QGSP\_INCLXX\_HP (since v10.0)
- FTFP\_INCLXX (since v10.0)
- FTFP\_INCLXX\_HP (since v10.0)

The \*\_HP variants use the NeutronHP model below 20 MeV to simulate neutron elastic and inelastic scattering using evaluated data libraries. The QGSP\_\* and FTFP\_\* variants respectively use the Quark-Gluon String model (QGS) and the Fritiof model (FTF) at high energy. For low-energy nucleon-induced reactions, the Precoumpound model is used below 1 MeV and INCL++ fades in between 1 and 2 MeV; the Binary-Cascade model is used for reactions between heavy nuclei. Bertini is used for reactions induced by kaons, which cannot be treated by INCL++ at the moment. A map of models (accurate as of Geant4 v10.0) is shown in Fig. 34. For further details about all the Geant4 models, the reader is referred to the Geant4 Physics Reference Manual [98].

#### 1. Recommendations for the choice of the de-excitation model in Geant4

We have shown (Sections III and IV) that fragmentation cross sections are very sensitive to the choice of the de-excitation model. Since Geant4 v10.0, it is possible to choose to couple INCL++ to G4ExcitationHandler (default) or to ABLA V3; therefore, we provide some guidelines for the users hereafter.

We can summarize some of the results presented in Secs. IVC and IVE. ABLA V3 describes rather well most of the observables connected with the de-excitation of heavy nuclei (say  $A \gtrsim 150$ ); this conclusion relies partly on the results of the present work (Figs. 25–27) and mostly on a large body of validation for nucleon-induced reactions [e.g. 23]. There are however a few observables that are not accounted for by ABLA V3, even on heavy systems, such as those connected with evaporation of deuterons, tritons,  $^3\text{He}$  or fragments with  $A > 5$ .

For light systems, we show below that G4ExcitationHandler often provides a better description of de-excitation than ABLA V3. In addition, G4ExcitationHandler provides de-excitation mechanisms for the evaporation of any fragment up to  $^{28}\text{Mg}$ . On

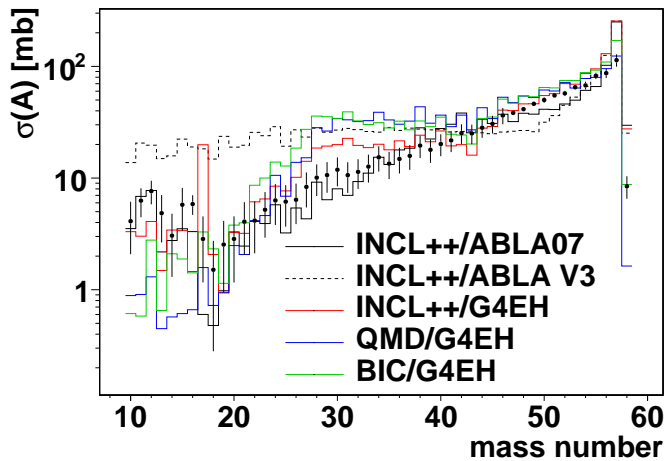


Figure 30. (Color online) Fragmentation cross sections for the 140-AMeV  $^{58}\text{Ni}+^9\text{Be}$  reaction, as a function of the fragment mass number. Model calculations are compared to the data taken from Refs. 91, 92. In the plot legend, *G4EH* stands for G4ExcitationHandler.

the other hand, G4ExcitationHandler’s fission sector performs less well than ABLA V3’s fission module when coupled with INCL++. Again, this is shown in the present paper (Fig. 25) but is also confirmed by an extensive private intercomparison.

We therefore recommend that users employ G4ExcitationHandler (the default choice) when they expect emphasis to be put on the de-excitation of light nuclei ( $A \lesssim 150$ ) and/or on specific observables that are most probably incorrectly described by ABLA V3 (such as tritium production). We recommend use of ABLA V3 when emphasis is to be put on fission. The Geant4 Application Developer Guide [99, section 5.2.2.4] describes the steps necessary to couple INCL++ to ABLA V3 within Geant4.

The present situation is clearly unsatisfactory insofar as none of the available de-excitation models yields good overall performance. The development of such a model is one of our development goals.

## 2. Newer INCL++ version in Geant4 v10.1 $\beta$

At the time of writing, a newer version of INCL++ (v5.2) has been distributed with the latest public release of Geant4 (v10.1 $\beta$ ). The essential difference with the model described by the present paper (v5.1.14) consists in the extension towards higher incident energies [100, 101]. This work had initially been carried out in the framework of an old Fortran version of INCL and has recently been merged in the Fortran development version and converted to C++ for inclusion in INCL++. The essential ingredient for the extension is the inclusion of new inelastic channels in the elementary nucleon-nucleon and pion-nucleon collisions. We do not introduce additional baryonic resonances (besides the narrow  $\Delta(1232)$ ) be-

cause they are largely overlapping and very short-lived, compared to the time between subsequent cascade collisions. Instead, the inelastic collisions are assumed to proceed directly to multiple-pion production. Final-state pion multiplicities up to 4 are considered, which pushes the high-energy limit of INCL++ v5.2 up to  $\sim 15$  GeV in nucleon- and pion-induced reactions. Note that the high-energy extension does not substantially modify the results of the code below  $\sim 1$  GeV. Further details are available in Refs. 100 and 101.

Figure 35 above shows a map of models for the INCL++-based physics lists in Geant4 v10.1 $\beta$ . INCL++ is used up to 15 GeV for pion- and nucleon-induced reactions, and it is gradually replaced by the relevant high-energy string model between 15 and 20 GeV.

An extensive verification of the new INCL++ version has been performed and will be the object of a future publication. As a sample of the quality of the new predictions, we show in Fig. 36 the calculations results for double-differential cross sections for pion production from 8-GeV/c  $p+^{181}\text{Ta}$ .

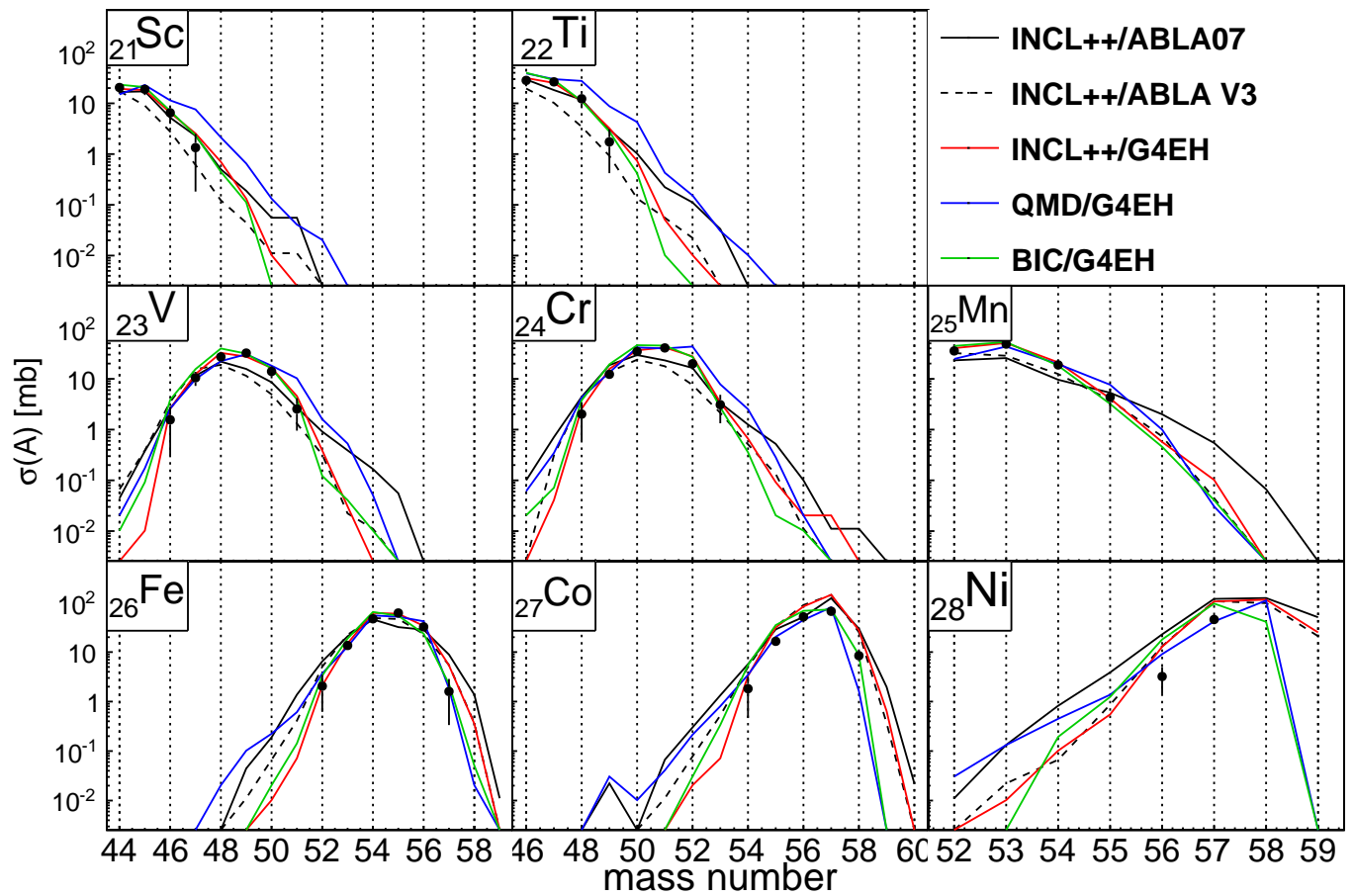


Figure 31. (Color online) Isotopic distributions ( $21 \leq Z \leq 28$ ) for the  $140\text{-AMeV } ^{58}\text{Ni} + ^9\text{Be}$  reaction. Model calculations are compared to the data taken from Refs. 91, 92. In the plot legend,  $G4EH$  stands for G4ExcitationHandler.

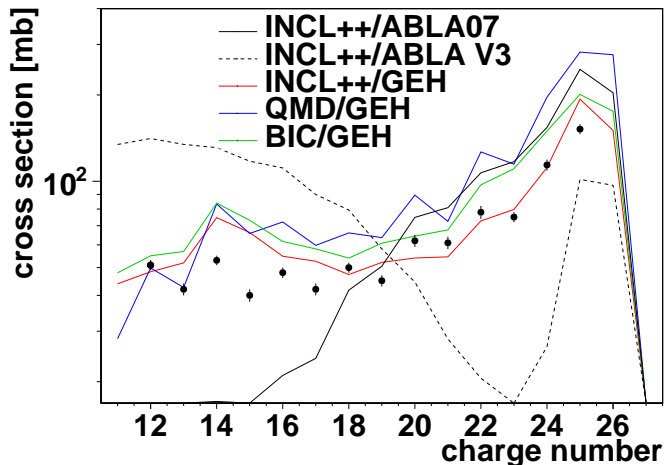


Figure 32. (Color online) Partial charge-changing cross sections for the 1.05-AGeV  $^{56}\text{Fe}+^{12}\text{C}$  reaction. Model calculations are compared to the data taken from Refs. 93.

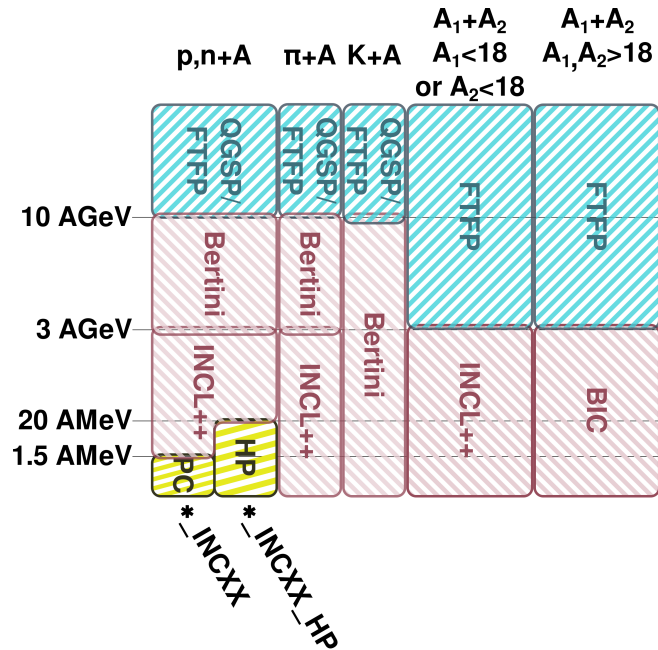


Figure 34. (Color online) Map of models used by the INCL++-based physics lists in Geant4 v10.0. Physics lists whose name ends in `_HP` use the NeutronHP model for neutron transport at low energies (represented as “HP” on the map); those starting with `QGSP_` (`FTFP_`) use the Quark-Gluon-String model (the Fritiof model) at high energy. “PC” stands for PreCompound.

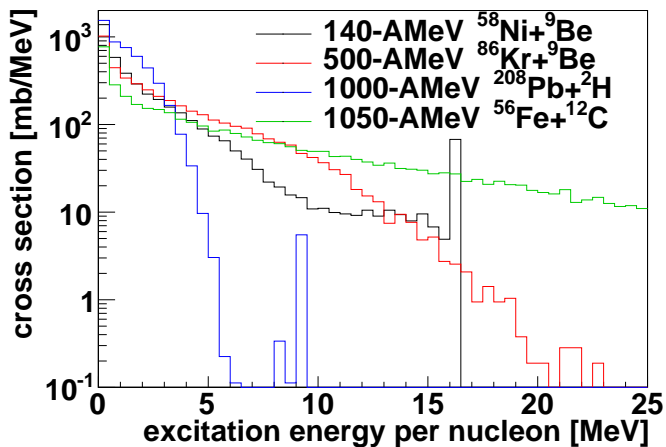


Figure 33. (Color online) Distributions of the excitation energy of the cascade remnants, as calculated by INCL++, for the reactions shown in this section.

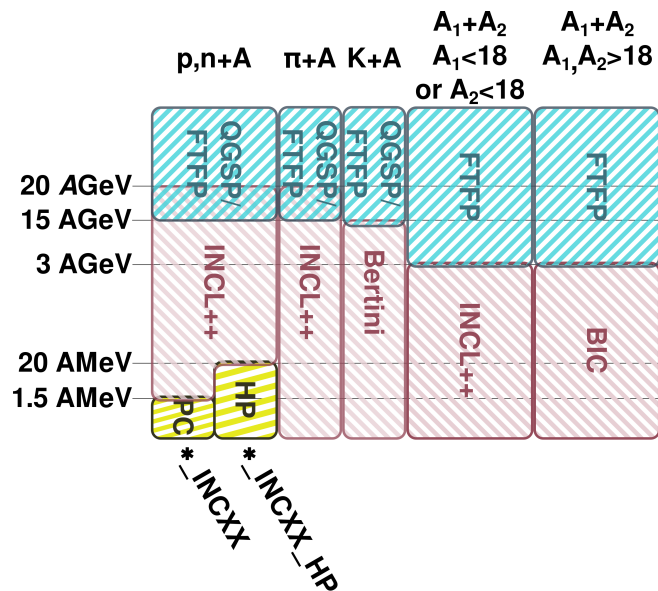


Figure 35. (Color online) Same as Fig. 34 for the INCL++-based physics lists in Geant4 v10.1 $\beta$ .



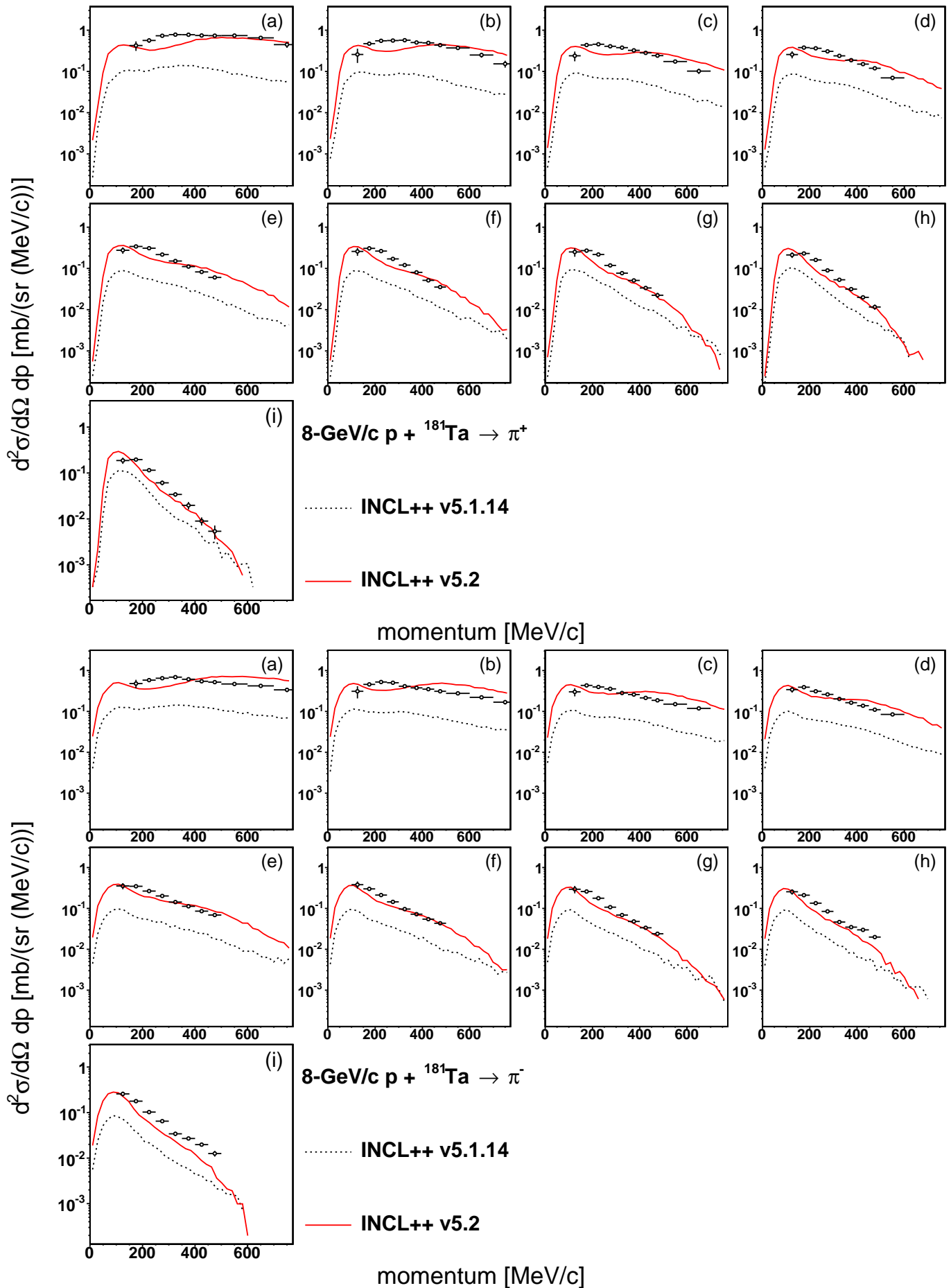


Figure 36. (Color online) Double-differential cross sections for the production of  $\pi^+$  (top) and  $\pi^-$  (bottom) at (a)  $25^\circ$ , (b)  $37^\circ$ , (c)  $48^\circ$ , (d)  $60^\circ$ , (e)  $71^\circ$ , (f)  $83^\circ$ , (g)  $94^\circ$ , (h)  $105^\circ$  and (i)  $117^\circ$  from a  $8\text{-GeV}/c \text{ p} + {}^{181}\text{Ta}$  reaction. The INCL++ calculations are compared to the data from Ref. 95.

- [1] G. Kraft, *Strahlenther. Onkol.* **166**, 10 (1990); *Prog. Part. Nucl. Phys.* **45**, S473 (2000).
- [2] K. Parodi, H. Paganetti, H. A. Shih, S. Michaud, J. S. Loeffler, T. F. DeLaney, N. J. Liebsch, J. E. Munzenrider, A. J. Fischman, A. Knopf, and T. Bortfeld, *Int. J. Radiat. Oncol. Biol. Phys.* **68**, 920 (2007).
- [3] W. Enghardt, J. Debus, T. Haberer, B. G. Hasch, R. Hinz, O. Jäkel, M. Krämer, K. Lauckner, J. Pawelke, and F. Pönisch, *Nucl. Phys. A* **654**, 1047c (1999).
- [4] M. Durante, *Riv. Nuovo Cimento* **25**, 1 (2002).
- [5] D. J. Morrissey and B. M. Sherrill, *Philos. T. Roy. Soc. A* **356**, 1985 (1998).
- [6] H. L. Ravn, *Philos. T. Roy. Soc. A* **356**, 1955 (1998).
- [7] A. Stolz, T. Faestermann, J. Friese, *et al.*, *Phys. Rev. C* **65**, 064603 (2002); J. Benlliure, T. Kurtukian-Nieto, L. Audouin, *et al.*, *Eur. Phys. J. Spec. Top.* **150**, 309 (2007); J. Benlliure, M. Fernández-Ordóñez, L. Audouin, *et al.*, *Phys. Rev. C* **78**, 054605 (2008); H. Alvarez-Pol, J. Benlliure, E. Casarejos, *et al.*, *Phys. Rev. C* **82**, 041602 (2010).
- [8] B. Blank, S. Andriamonje, R. Del Moral, *et al.*, *Phys. Rev. C* **50**, 2398 (1994); J. Kurcewicz, Z. Liu, M. Pfützner, *et al.*, *Nucl. Phys. A* **767**, 1 (2006).
- [9] P. Hansen and J. Tostevin, *Annu. Rev. Nucl. Part. S.* **53**, 219 (2003).
- [10] L. Audirac, A. Obertelli, P. Doornenbal, *et al.*, *Phys. Rev. C* **88**, 041602 (2013).
- [11] L. Sihver and D. Mancusi, *Radiat. Meas.* **44**, 38 (2009).
- [12] J. W. Wilson, F. F. Badavi, F. A. Cucinotta, J. Shinn, G. D. Badhwar, R. Silberberg, C. Tsao, L. W. Townsend, and R. K. Tripathi, *HZETRN: description of a free-space ion and nucleon transport and shielding computer program*, Tech. Rep. TP-3495 (NASA, 1995).
- [13] M. Krämer, O. Jäkel, T. Haberer, G. Kraft, D. Scharadt, and U. Weber, *Phys. Med. Biol.* **45**, 3299 (2000).
- [14] D. Filges and F. Goldenbaum, *Handbook of spallation research. Theory, experiments and applications* (Wiley-VCH, Berlin, 2009).
- [15] V. E. Bunakov and G. V. Matvejev, *Z. Phys. A* **322**, 511 (1985).
- [16] A. Boudard, J. Cugnon, J.-C. David, S. Leray, and D. Mancusi, *Phys. Rev. C* **87**, 014606 (2013), arXiv:1210.3498 [nucl-th].
- [17] A. Kelić, M. V. Ricciardi, and K.-H. Schmidt, in [102], p. 181, report INDC(NDC)-0530.
- [18] S. Leray, J.-C. David, M. Khandaker, G. Mank, A. Mengoni, N. Otsuka, D. Filges, F. Gallmeier, A. Konobeyev, and R. Michel, *J. Korean Phys. Soc.* **59**, 791 (2011); “IAEA benchmark of spallation models,” <http://www-nds.iaea.org/spallations>.
- [19] P. Kaitaniemi, A. Boudard, S. Leray, J. Cugnon, and D. Mancusi, *Prog. Nucl. Sci. Technol.* **2**, 788 (2011).
- [20] P. K. A. de Witt Huberts, *J. Phys. G: Nucl. Part. Phys.* **16**, 507 (1990).
- [21] Y. Yariv and Z. Fraenkel, *Phys. Rev. C* **20**, 2227 (1979).
- [22] Y. Yariv and Z. Fraenkel, *Phys. Rev. C* **24**, 488 (1981).
- [23] A. Boudard, J. Cugnon, S. Leray, and C. Volant, *Phys. Rev. C* **66**, 044615 (2002).
- [24] M. Lacombe, B. Loiseau, J. Richard, R. V. Mau, J. Côté, P. Pirès, and R. de Tournel, *Phys. Lett. B* **101**, 139 (1981).
- [25] H. D. Vries, C. W. D. Jager, and C. D. Vries, *Atom. Data Nucl. Data* **36**, 495 (1987).
- [26] The exact masses of the outgoing nucleons are recovered by applying a correction that involves the empirical particle-emission thresholds [16].
- [27] W. Shen, B. Wang, J. Feng, W. Zhan, Y. Zhu, and E. Feng, *Nucl. Phys. A* **491**, 130 (1989).
- [28] J. K. Tuli *et al.*, “Nuclear wallet cards,” <http://www.nndc.bnl.gov/wallet/> (2005).
- [29] T. Aoust and J. Cugnon, *Eur. Phys. J. A* **21**, 79 (2004).
- [30] J. Galin, D. Guerreau, M. Lefort, and X. Tarrago, *Phys. Rev. C* **9**, 1018 (1974).
- [31] R. Bass, *Nucl. Phys. A* **231**, 45 (1974).
- [32] D. Mancusi, K. Niita, T. Maruyama, and L. Sihver, *Phys. Rev. C* **79**, 014614 (2009), doi: 10.1103/PhysRevC.79.014614.
- [33] J.-J. Gaimard and K.-H. Schmidt, *Nucl. Phys. A* **531**, 709 (1991); A. Junghans, M. de Jong, H.-G. Clerc, A. Ignatyuk, G. Kudyaev, and K.-H. Schmidt, **629**, 635 (1998); C++ translation by C. Schmitt.
- [34] E. Fermi, *Prog. Theor. Phys.* **5**, 570 (1950).
- [35] A. P. Zhdanov and P. I. Fedotov, *Sov. Phys. JETP* **18**, 313 (1964).
- [36] B. V. Carlson, R. Donangelo, S. R. Souza, W. G. Lynch, A. W. Steiner, and M. B. Tsang, *Nucl. Phys. A* **876**, 77 (2012).
- [37] J. M. Quesada, V. Ivanchenko, A. Ivanchenko, M. A. Cortés-Giraldo, G. Folger, A. Howard, and D. Wright, *Prog. Nucl. Sci. Technol.* **2**, 936 (2011).
- [38] S. G. Mashnik and L. M. Kerby, *Nucl. Instrum. Meth. A* **764**, 59 (2014).
- [39] T. Goorley, M. James, T. Booth, *et al.*, *Nucl. Technol.* **180**, 298 (2012).
- [40] D. R. F. Cochran, P. N. Dean, P. A. M. Gram, E. A. Knapp, E. R. Martin, D. E. Nagle, R. B. Perkins, W. J. Shlaer, H. A. Thiessen, and E. D. Theriot, *Phys. Rev. D* **6**, 3085 (1972).
- [41] S. Leray *et al.*, *Phys. Rev. C* **65**, 044621 (2002).
- [42] W. B. Amian, R. Byrd, C. A. Goulding, M. M. Meier, G. L. Morgan, C. E. Moss, and D. A. Clark, *Nucl. Sci. Eng.* **112**, 78 (1992).
- [43] T. Enqvist, W. Wlazole, P. Armbruster, *et al.*, *Nucl. Phys. A* **686**, 481 (2001).
- [44] A. Kelić, K.-H. Schmidt, T. Enqvist, *et al.*, *Phys. Rev. C* **70**, 064608 (2004).
- [45] D. Ashery, I. Navon, G. Azuelos, H. K. Walter, H. J. Pfeiffer, and F. W. Schlepütz, *Phys. Rev. C* **23**, 2173 (1981).
- [46] C. J. Gelderloos, J. T. Brack, M. D. Holcomb, M. V. Keilman, D. J. Mercer, R. J. Peterson, R. A. Ristinen, and A. Saunders, *Phys. Rev. C* **62**, 024612 (2000).
- [47] F. Binon, P. Duteil, J. P. Garron, J. Gorres, L. Hugon, J. P. Peigneux, C. Schmit, M. Spighel, and J. P. Stroot, *Nucl. Phys. B* **17**, 168 (1970).
- [48] M. Crozon, P. Chavanon, A. Courau, T. Leray, J. L. Narjoux, and J. Tocqueville, *Nucl. Phys.* **64**, 567 (1965).
- [49] R. D. McKeown, S. J. Sanders, J. P. Schiffer, H. E. Jackson, M. Paul, J. R. Specht, E. J. Stephenson, R. P. Redwine, and R. E. Segel,

- Phys. Rev. Lett. **44**, 1033 (1980).
- [50] Y. Iwamoto, N. Shigyo, D. Satoh, S. Kunieda, T. Watanabe, S. Ishimoto, H. Tenzou, K. Maehata, K. Ishibashi, T. Nakamoto, M. Numajiri, S. Meigo, and H. Takada, Phys. Rev. C **70**, 024602 (2004).
- [51] We remind the reader that the production of the  $\Delta$  resonance is the only open channel for pions in INCL4.6 and INCL++ v5.1.14.
- [52] A. Auce, R. F. Carlson, A. J. Cox, A. Ingemarsson, R. Johansson, P. U. Renberg, O. Sundberg, and G. Tibell, Phys. Rev. C **53**, 2919 (1996).
- [53] L. V. Dubar, O. F. Nemets, L. I. Slyusarenko, and V. V. Tokarevskii, Yad. Fiz. **20**, 624 (1974).
- [54] R. C. Brown, A. A. Debenham, J. A. R. Griffith, O. Karban, D. C. Kocher, and S. Roman, Nucl. Phys. A **208**, 589 (1973).
- [55] K. Bearpark, W. R. Graham, and G. Jones, Nucl. Instrum. Meth. **35**, 235 (1965).
- [56] B. Bonin, N. Alamanos, B. Berthier, G. Bruge, H. Faraggi, J. C. Lugol, W. Mittig, L. Papineau, A. I. Yavin, J. Arvieux, L. Farvacque, M. Buenerd, and W. Bauhoff, Nucl. Phys. A **445**, 381 (1985).
- [57] A. Auce, R. F. Carlson, A. J. Cox, A. Ingemarsson, R. Johansson, P. U. Renberg, O. Sundberg, G. Tibell, and R. Zorro, Phys. Rev. C **50**, 871 (1994).
- [58] A. Ingemarsson, J. Nyberg, P. U. Renberg, O. Sundberg, R. F. Carlson, A. J. Cox, A. Auce, R. Johansson, G. Tibell, D. T. Khoa, and R. E. Warner, Nucl. Phys. A **676**, 3 (2000).
- [59] Y. Nagame, Y. Nakamura, M. Takahashi, K. Sueki, and H. Nakahara, Nucl. Phys. A **486**, 77 (1988).
- [60] Z. Szucs, F. Szelecsenyi, J. Bergman, S.-J. Heselius, and O. Solin, Radiochim. Acta **65**, 87 (1994).
- [61] O. N. Vysotsky, A. V. Gonchar, G. N. Kozeratskaya, S. N. Kondratev, V. D. Sklyarenko, and V. V. Tokarevsky, B. Russ. Acad. Sci. Phys. **56**, 718 (1992).
- [62] S. G. Mashnik, K. K. Gudima, R. E. Prael, *et al.*, in [102], p. 51, report INDC(NDC)-0530, arXiv:0805.0751 [nucl-th].
- [63] S. G. Mashnik, R. J. Peterson, A. J. Sierk, and M. R. Braunstein, Phys. Rev. C **61**, 034601 (2000).
- [64] H. Iwase, Y. Iwata, T. Nakamura, K. Gudima, S. Mashnik, A. Sierk, and R. Prael, AIP Conf. Proc. **769**, 1066 (2005).
- [65] Mashnik, Stepan G., Kerby, Leslie M., Gudima, Konstantin K., and Sierk, Arnold J., EPJ Web of Conferences **66**, 03059 (2014), arXiv:1306.6547 [nucl-th].
- [66] S. G. Mashnik, K. K. Gudima, R. E. Prael, and A. J. Sierk, in *Proceedings of the Workshop on Nuclear Data for the Transmutation of Nuclear Waste*, edited by A. Kelić and K.-H. Schmidt (GSI, Darmstadt, Germany, 2003) arXiv:0404018 [nucl-th].
- [67] S. G. Mashnik, K. K. Gudima, N. V. Mokhov, and R. E. Prael, *LAQGSM03.03 upgrade and its validation*, LANL report LA-UR-07-6198 (Los Alamos National Laboratory, 2007) arXiv:0709.1736 [nucl-th].
- [68] N. V. Mokhov, K. K. Gudima, and S. I. Striganov, in *Shielding Aspects of Accelerators, Targets and Irradiation Facilities - SATIF 11 Workshop Proceedings* (OECD Publishing, Tsukuba, Japan, 2012).
- [69] M. Takechi, M. Fukuda, M. Mihara, *et al.*, Phys. Rev. C **79**, 061601 (2009).
- [70] M. Fukuda, M. Takechi, D. Nishimura, *et al.*, in *Tours symposium on nuclear physics and astrophysics — VII*, AIP Conf. Proc., Vol. 1238 (AIP, Kobe, Japan, 2009) pp. 270–273.
- [71] M. Takechi, *Elucidation of the behavior of reaction cross sections at intermediate energies and halo structure of  ${}^6\text{He}$* , Ph.D. thesis, Osaka University (2006).
- [72] M. Takechi, M. Fukuda, M. Mihara, *et al.*, Eur. Phys. J. A **25**, 217 (2005).
- [73] S. Kox, A. Gamp, C. Perrin, J. Arvieux, R. Bertholet, J. F. Bruandet, M. Buenerd, Y. El Masri, N. Longequeue, and F. Merchez, Phys. Lett. B **159**, 15 (1985).
- [74] S. Kox, A. Gamp, R. Cherkaoui, A. J. Cole, N. Longequeue, J. Menet, C. Perrin, and J. B. Viano, Nucl. Phys. A **420**, 162 (1984).
- [75] Y. Iwata, T. Murakami, H. Sato, H. Iwase, T. Nakamura, T. Kurosawa, L. Heilbronn, R. M. Ronningen, K. Ieki, Y. Tozawa, and K. Niita, Phys. Rev. C **64**, 054609 (2001).
- [76] E. J. Moniz, I. Sick, R. R. Whitney, J. R. Ficenc, R. D. Kephart, and W. P. Trower, Phys. Rev. Lett. **26**, 445 (1971).
- [77] L. Heilbronn, C. J. Zeitlin, Y. Iwata, T. Murakami, H. Iwase, T. Nakamura, T. Nunomiya, H. Sato, H. Yashima, R. M. Ronningen, and K. Ieki, Nucl. Sci. Eng. **157**, 142 (2007).
- [78] J. Dudouet, D. Juliani, M. Labalme, *et al.*, Nucl. Instrum. Meth. A **715**, 98 (2013), experimental data retrieved on 13<sup>th</sup> December 2013 from <http://hadrontherapy-data.in2p3.fr/>.
- [79] G. Folger, V. Ivanchenko, and J. Wellisch, Eur. Phys. J. A **21**, 407 (2004).
- [80] A. Heikkinen, N. Stepanov, and J. P. Wellisch, in *Proceedings to Computing in High Energy and Nuclear Physics 2003 (CHEP03)* (La Jolla, CA, U.S.A., 2003) p. MOMT008, arXiv:0306008 [nucl-th].
- [81] M. Kelsey, D. Wright, *et al.*, in preparation (2014).
- [82] K. K. Gudima, S. G. Mashnik, and V. D. Toneev, Nucl. Phys. A **401**, 329 (1983).
- [83] J. Dudouet, D. Juliani, M. Labalme, *et al.*, Phys. Rev. C **88**, 024606 (2013).
- [84] J. Dudouet, D. Cussol, D. Durand, and M. Labalme, Phys. Med. Biol. (2014), submitted, arXiv:1309.1544 [nucl-ex].
- [85] P. Napolitani, K.-H. Schmidt, A. S. Botvina, F. Rejmund, L. Tassan-Got, and C. Villagrasa, Phys. Rev. C **70**, 054607 (2004).
- [86] J. Benlliure, P. Armbruster, M. Bernas, A. Boudard, J. P. Dufour, T. Enqvist, R. Legrain, S. Leray, B. Mustapha, F. Rejmund, K.-H. Schmidt, C. Stéphan, L. Tassan-Got, and C. Volant, Nucl. Phys. A **683**, 513 (2001).
- [87] T. Enqvist, P. Armbruster, J. Benlliure, *et al.*, Nucl. Phys. A **703**, 435 (2002).
- [88] J. Cugnon, T. Aoust, and A. Boudard, in *Seminar on Fission VI*, edited by C. Wagemans, J. Wagemans, and P. D'Hondt (2008).
- [89] B. Jurado, C. Schmitt, K.-H. Schmidt, J. Benlliure, and A. R. Junghans, Nucl. Phys. A **757**, 329 (2005).
- [90] M. Weber, C. Donzaud, J. Dufour, *et al.*, Nucl. Phys. A **578**, 659 (1994).
- [91] M. Mocko, M. B. Tsang, L. Andronenko, *et al.*, Phys. Rev. C **74**, 054612 (2006).
- [92] M. Mocko, *Rare isotope production*, Ph.D. thesis, Michigan State University, East Lansing, MI, U.S.A. (2006).

- [93] C. Zeitlin, L. Heilbronn, J. Miller, S. E. Rademacher, T. Borak, T. R. Carter, K. A. Frankel, W. Schimmerling, and C. E. Stronach, *Phys. Rev. C* **56**, 388 (1997).
- [94] D. Mancusi, A. Boudard, J. Cugnon, J.-C. David, T. Gorbinet, and S. Leray, *Phys. Rev. C* **84**, 064615 (2011), arXiv:1110.6343 [nucl-th].
- [95] M. G. Catanesi, E. Radicioni, R. Edgecock, *et al.* (HARP Collaboration), *Phys. Rev. C* **77**, 055207 (2008).
- [96] Y. Watanabe and D. N. Kadrev, *Radiat. Prot. Dosim.* **126**, 40 (2007).
- [97] S. Furihata, *Nucl. Instrum. Meth. B* **171**, 251 (2000).
- [98] *Geant4 Physics Reference Manual*, Geant4 collaboration (2013), version 10.0.
- [99] *Geant4 Application Developer Guide*, Geant4 collaboration (2013), version 10.0.
- [100] S. Pedoux, *Extension of the Liège intranuclear cascade model to the 2–15 GeV incident energy range*, Ph.D. thesis, University of Liège, Liège, Belgium (2011).
- [101] S. Pedoux and J. Cugnon, *Nucl. Phys. A* **866**, 16 (2011).
- [102] *Joint ICTP-IAEA Advanced Workshop on Model Codes for Spallation Reactions* (IAEA, Trieste, Italy, 2008) report INDC(NDC)-0530.